

Between Synchrony and Turbulence: Intricate Hierarchies of Coexistence Patterns

Sindre W. Haugland, Anton Tosolini, and Katharina Krischer^{a)}

Physics Department, Nonequilibrium Chemical Physics, Technical University of Munich, James-Frank-Str. 1, D-85748 Garching, Germany

(Dated: 30 December 2021)

Coupled oscillators, even identical ones, display a wide range of behaviours, among them synchrony and incoherence. The 2002 discovery of so-called chimera states, states of coexisting synchronized and unsynchronized oscillators, provided a possible link between the two and definitely showed that different parts of the same ensemble can sustain qualitatively different forms of motion. Here, we demonstrate that globally coupled identical oscillators can express a range of coexistence patterns more comprehensive than chimeras. A hierarchy of such states evolves from the fully synchronized solution in a series of cluster-splittings. At the far end of this hierarchy, the states further collide with their own mirror-images in phase space – rendering the motion chaotic, destroying some of the clusters and thereby producing even more intricate coexistence patterns. A sequence of such attractor collisions can ultimately lead to full incoherence of only single asynchronous oscillators. Chimera states, with one large synchronized cluster and else only single oscillators, are found to be just one step in this transition from low- to high-dimensional dynamics.

One of the big problems in physics is how high-dimensional disorder in space and time may emerge from a spatially ordered, in the simplest case uniform, state with low-dimensional dynamics¹. Exploring different paths from order to spatiotemporal disorder and their universal character is central for a deeper understanding of complex emergent behaviour such as spatiotemporal chaos in reaction-diffusion systems^{2,3} or turbulence in hydrodynamic flows^{4,5}.

Ensembles of coupled oscillators are one class of apparently simple dynamical systems that yet may adopt states ranging from full synchrony to complete incoherence, and which has provided insights in virtually any discipline, ranging from the natural sciences to sociology^{6,7}. During the last two decades, a kind of hybrid phenomenon, in which synchronized and incoherent oscillators coexist in an ensemble of identical oscillators⁸, coined a chimera state⁹, has received considerable attention (see Reviews^{10–12} and the references therein), not least since it can be considered a “natural link between coherence and incoherence”¹³. In an earlier study employing globally coupled logistic maps¹⁴, four different classes of behaviour were found, including a large variety of partially ordered states, some of which were later classified as chimeras¹⁵. Yet, the bifurcation structure between the different classes was not resolved.

In this article, we study the bifurcations from synchrony, via clustered and partially clustered states to full incoherence in a system of globally coupled oscillators with nonlinear coupling, with simulations and bifurcation analysis for an increasing number of oscillators. Here, chimera states are just one of a multitude of coexistence patterns, all consisting of clusters, that is, internally synchronized groups of oscillators, of widely different sizes

and dynamics, and possibly including one or several single oscillators. The path towards complete incoherence begins with a symmetry-breaking cascade of cluster-splitting period-doubling bifurcations, wherein the currently smallest cluster is repeatedly split into two, leading to hierarchical clustering. Due to the high symmetry of the system, each symmetry-breaking produces many equivalent mirror-image variants of each outcome state, multiplying the number of attractors and leading to an ever more crowded phase space¹⁶. At some point, each variant collides with some of its mirror-images, creating larger attractors with higher symmetry. Usually, this blows up some of the clusters, the resulting single oscillators henceforth moving similarly on average. A succession of such symmetry-increasing bifurcations destroys first the smallest clusters, and then the larger ones, partially mirroring the former cluster-splitting cascade and ultimately creating a completely incoherent state. A chimera state, consisting of one synchronized cluster and otherwise only single, incoherent oscillators is often the second to last state of the sequence.

The model we employ is an ensemble of N Stuart-Landau oscillators $W_k \in \mathbb{C}$, $k = 1, \dots, N$, with nonlinear global coupling¹⁷:

$$\frac{dW_k}{dt} = W_k - (1 + ic_2)|W_k|^2 W_k - (1 + i\nu)\langle W \rangle + (1 + ic_2)\langle |W|^2 W \rangle, \quad (1)$$

where c_2 and ν are real parameters and $\langle \dots \rangle = 1/N \sum_{k=1}^N \dots$ denotes ensemble averages. The Stuart-Landau oscillator itself is a generic model for a system close to a Hopf bifurcation, that is, to the onset of self-sustained oscillations¹⁸. Networks of such oscillators have previously been found to exhibit a wide range of dynamics, many of them occurring for linear global coupling^{19–23}. The nonlinear global coupling in equation (1) stands out by featuring two qualitatively different chimera states,

^{a)}Electronic mail: krischer@tum.de

each of them deduced to somehow emerge from a corresponding type of two-cluster solution²⁴. Originally, this coupling was inspired by electrochemical experiments, wherein the oxide layer on a silicon electrode displays a wide range of spatiotemporal patterns¹⁷. A few experimental measurements reminiscent of new results in equation (1) will be discussed later in this article.

Because the oscillators are identical and the coupling is global, the system is \mathbb{S}_N -equivariant: If $\mathbf{W}(t) \in \mathbb{C}^N$ is a solution, then so is $\gamma\mathbf{W}(t) \forall \gamma \in \mathbb{S}_N$, where \mathbb{S}_N is the *symmetric group* of all permutations of the N oscillators²⁵. Or in less mathematical terms: If we start at a solution to equation (1) and interchange the trajectories of any two oscillators, the result is still a solution. Further, the average $\langle W \rangle$ is confined to simple harmonic motion with frequency ν , as shown by taking the ensemble average of the whole equation:

$$\left\langle \frac{dW_k}{dt} \right\rangle = \frac{d}{dt} \langle W \rangle = -i\nu \langle W \rangle \Rightarrow \langle W \rangle = \eta e^{-i\nu t}, \quad (2)$$

where $\eta \in \mathbb{R}$ is an additional parameter, implicitly set by choosing the initial condition. This constraint also implies that for a Poincaré map²⁶ defined by sampling the system with frequency ν , the average of the N components of the map will always be constant. Thus the nonlinear constraint in the time-continuous equation (1) becomes a linear constraint in the time-discrete map.

RESULTS

The fully synchronized solution $W_k = \eta e^{-i\nu t} \forall k$ always exists and is stable for sufficiently large values of η . It loses stability in either an equivariant pitchfork bifurcation, producing separate clusters that continue to orbit the origin with frequency ν at different fixed amplitudes, or an equivariant Hopf bifurcation to a T^2 torus, producing separate modulated-amplitude clusters that henceforth oscillate with two superposed frequencies ν and ω_H ²⁷. We will focus on the latter and the dynamics arising from these.

The equivariant Hopf bifurcation occurs at $\eta_H = 1/\sqrt{2}$ for suitable values of c_2 and ν . For $\nu = 0.1$, which we keep fixed throughout, it does for $c_2 < -0.448$ ¹⁷. In this Hopf bifurcation, differently balanced two-cluster solutions ranging from $(N-1) - 1$ (with all but one oscillator in the largest cluster) to $N/2 - N/2$ (with half the oscillators in each cluster) emerge from the synchronized solution. Some of these emerge as stable and others as unstable, depending on the value of c_2 . The balanced $N/2 - N/2$ solution, with an equal number of oscillators in each cluster, is shown in Fig. 1 a-b. The dashed circle marks the enforced path of the ensemble average $\langle W \rangle = \eta e^{-i\nu t}$, which the two clusters orbit on opposite sides as it circles the origin. An unbalanced $3N/4 - N/4$ solution, with $N_1 = 3N/4$ of the oscillators in one cluster and $N_2 = N/4$ in the other, looks as in Fig. 1 c-d.

Because $\langle W \rangle$ is independent of the individual oscillator dynamics, the value of any oscillator in the frame of reference of the ensemble average is always given by the simple transformation

$$W_k = \eta e^{-i\nu t} (1 + w_k) \Rightarrow w_k = W_k \eta^{-1} e^{i\nu t} - 1, \quad (3)$$

where w_k is the value of W_k in the co-rotating frame. There, the $N/2 - N/2$ solution from Fig. 1 a-b is simply periodic with frequency ω_H and looks as in Fig. 1 e-f. An unbalanced modulated-amplitude $3N/4 - N/4$ solution like that in Fig. 1 c-d appears as in Fig. 1 g-h. The average of all oscillators in the co-rotating frame of $\langle W \rangle$ is of course always zero. Notably, the global coupling ensures that all solutions for an ensemble size N are also solutions for $N' = nN$, $n \in \mathbb{N}$, with every cluster scaled up by a factor of n . For solutions that contain only clusters $N_i \geq 2$, the stability properties will also be the same for different n ^{22,28}.

If we initialize the $N/2 - N/2$ solution at a point in the $c_2 - \eta$ parameter plane where it is stable and from there on gradually change c_2 and/or η appropriately, one of the two clusters will break up into two smaller clusters. A possible outcome is shown in Fig. 1 i-j. The trajectory of the two new clusters is no longer simply periodic, but period-2, with a small and a large loop. The $N/2 - N/2$ solution has thus become unstable in a symmetry-breaking period-doubling bifurcation, giving rise to a stable $N/2 - N/4 - N/4$ three-cluster solution. This bifurcation also destabilizes less balanced two-cluster solutions, such as the $3N/4 - N/4$ solution in Fig. 1 g-h. In these cases, the smaller of the two clusters is split. The position of the period-doubling bifurcation in parameter space depends on the relative sizes of the clusters, as shown by the blue line in Fig. 1 k, which tracks the value of c_2 at which this bifurcation occurs as a function of N_1/N for $\eta = 0.67$.

For very unbalanced solutions $N_1/N > 0.8$, the smallest cluster is destroyed in a subcritical pitchfork bifurcation (green line). This results in several smaller clusters and/or single oscillators, depending on the relative sizes of the initial two clusters. In some cases, a few oscillators originally in the smaller cluster are also absorbed by the larger one. As the transition is subcritical, these outcome states are not directly related to the initial two-cluster solution, but rather belong to a different, coexisting solution branch. They will not concern us further here.

Hierarchical clustering through pervasive stepwise symmetry breaking

If we concentrate on the $N/2 - N/2$ solution, that is, keep $N_1/N = 0.5$ fixed, we can track the cluster-splitting period-doubling bifurcation in both c_2 and η simultaneously. A part of the resultant bifurcation line in the $c_2 - \eta$ parameter plane is delineated by the leftmost line in Fig. 2 c. Beyond this bifurcation, we find a mesh of

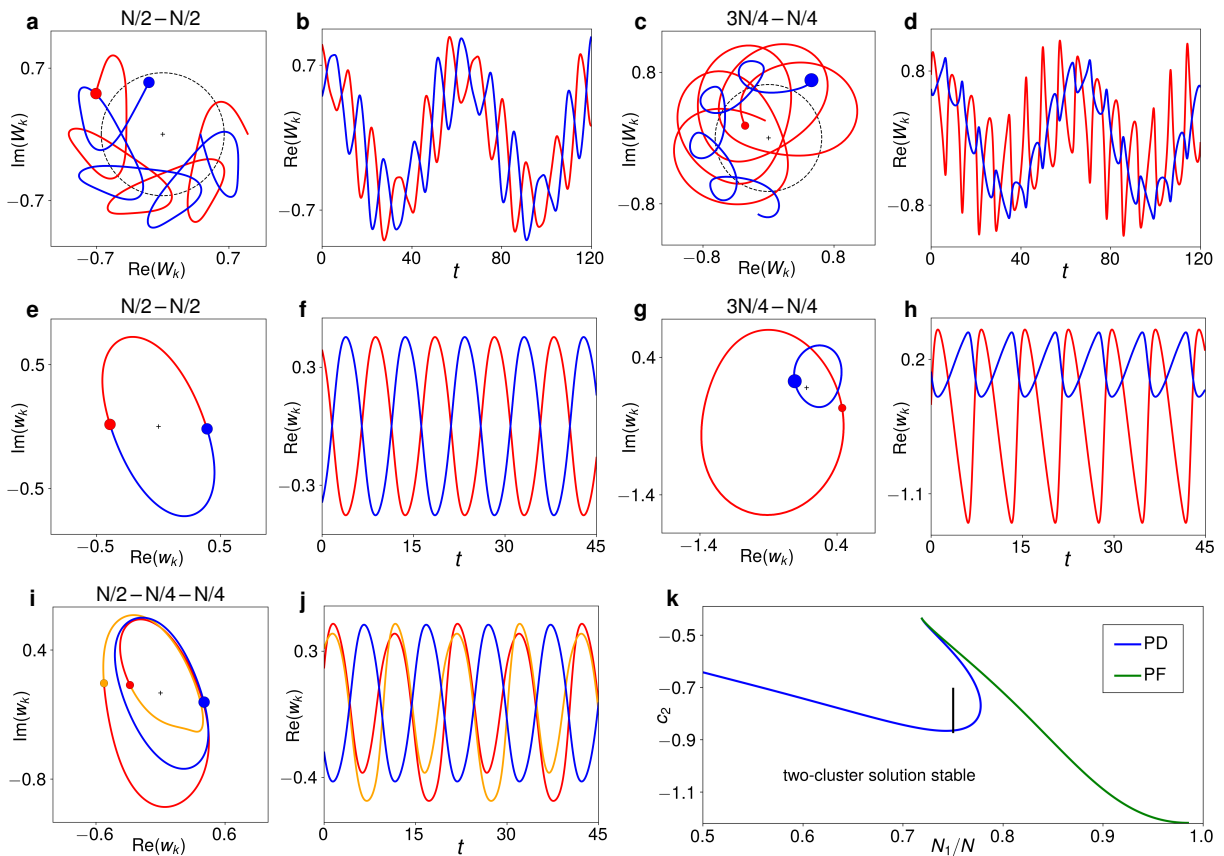


FIG. 1. **Two-cluster solutions and their bifurcations.** **a** Trajectory of an $N/2-N/2$ modulated-amplitude cluster solution for $c_2 = -0.71$ and $\eta = 0.65$. **b** Time series of the real part of each oscillator in **a**. **c-d** Like **a-b** for an unbalanced $3N/4-N/4$ solution at $c_2 = -1.0$ and $\eta = 0.65$. **e-h** The solutions in **a-b** and **c-d**, respectively, when viewed in a frame co-rotating with the ensemble average $\langle W \rangle = \eta e^{-i\Omega t}$. For the $N/2-N/2$ solution, the two clusters follow the same trajectory. **i-j** $N/2-N/4-N/4$ three-cluster solution at $c_2 = -0.69$, emerging from the solution in **a-b** in a period-doubling bifurcation. **k** Bifurcations destabilizing the two-cluster solution as a function of c_2 and the relative size of the larger cluster N_1/N for $\eta = 0.67$. The blue line denotes a period-doubling (PD) that splits the smaller cluster, and the green line a subcritical pitchfork (PF) that blows it up. The vertical black line marks the c_2 -incremented simulation in Fig. 6.

additional cluster-splitting bifurcation curves, creating a hierarchy of successively less symmetric multi-cluster solutions with various periodicities. Each bifurcation involves the breakup of either one cluster or two similarly behaving clusters and produces several qualitatively different solutions, differing by how the oscillators of the splitting cluster(s) distribute. (For example, the $4-4$ solution for $N = 8$ can split into either $4-2-2$, $4-3-1$, $2-2-2-2$, $2-2-3-1$ or $3-1-3-1$.) However, all these solutions will usually not be co-stable.

Fig. 2c shows the stability boundaries of several solutions for $N = 16$. The $N/2-N/2 = 8-8$ solution is stable in the upper left. This solution is destabilized at the leftmost blue period-doubling line. When increasing c_2 past this line for $\eta > 0.635$ (that is, in the upper half of the figure), it gives rise to stable $8-4-4$ and $8-5-3$ solutions (shown in Figs. 1i-j and 2a, respectively). The $8-5-3$ solution is stable within the two dashed lines. Be-

low the dashed green line, this solution in turn produces a stable $5-3-5-3$ and unstable $5-3-6-2$ and $5-3-7-1$ solutions. At the dashed blue line, it undergoes another period-doubling cluster split to an $8-5-2-1$ period-4 solution.

Between $\eta = 0.62$ and $\eta = 0.635$, only the $8-4-4$ solution emerges as stable when crossing the leftmost period-doubling line. The remaining solid bifurcation lines all affect this solution and its descendants. At the solid green line from $c_2 \approx -0.755$ to $c_2 \approx -0.725$ in the lower left, it produces stable $4-4-4-4$ and $4-4-5-3$ (Fig. 2b) solutions, as well as unstable $4-4-6-2$ and $4-4-7-1$ solutions. Like the dashed green line, this is an equivariant pitchfork bifurcation, splitting clusters, but not altering the overall periodicity of the ensemble. Below this pitchfork line, the above-mentioned $4-4-4-4$, $4-4-5-3$, $4-4-6-2$ and $4-4-7-1$ four-cluster solutions also emerge directly from the $8-8$ solution at the leftmost

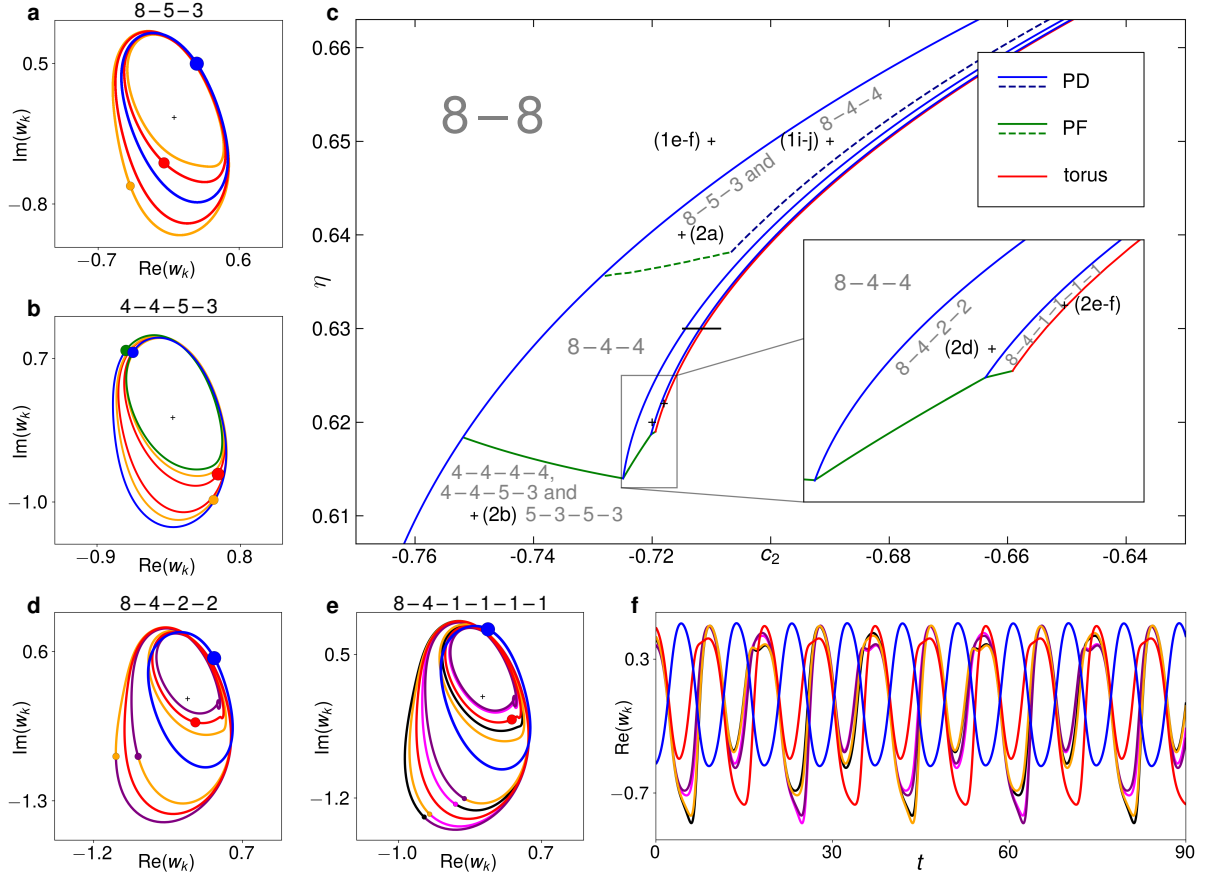


FIG. 2. **Cluster solutions and bifurcations for $N = 16$.** Sizes of filled circles mirror sizes of clusters. **a** 8-5-3 solution in the co-rotating frame of $\langle W \rangle$ for $c_2 = -0.715$ and $\eta = 0.64$. **b** 4-4-5-3 solution for $c_2 = -0.75$ and $\eta = 0.61$. **c** Bifurcation diagram of 8-8-derived solutions with PD=period-doubling, PF=pitchfork. Dashed lines mark bifurcations of the 8-5-3 solution (a), solid lines those of the 8-4-4 (Fig. 1 i-j) and the solutions emerging from it. Grey labels mark where each type of solution is stable. Labeled crosses mark the parameter values of the solutions depicted in Figs. 1 e-f, 1 i-j, **a-b** and **d-f**. The black line marks the c_2 -incremented simulation in Fig. 3 a-b. **d** 8-4-2-2 solution for $c_2 = -0.72$ and $\eta = 0.62$. **e-f** 8-4-1-1-1-1 solution for $c_2 = -0.718$ and $\eta = 0.62$, including time series of real part of each cluster and single oscillator.

period-doubling line.

At the solid blue line directly to the right of the dashed blue one, the 8-4-4 solution undergoes a period-doubling bifurcation analogous to that of the 8-5-3 solution, producing a stable 8-4-2-2 (Fig. 2 d) and an unstable 8-4-3-1 period-4 solution. The former becomes unstable either at the bottom diagonal green pitchfork line at $c_2 \approx -0.72$ or at the rightmost blue period-doubling line. In the latter case (see inset), the 8-4-2-2 solution produces an unstable 8-4-2-1-1 and a stable 8-4-1-1-1-1 period-8 solution (Fig. 2e-f).

At the red line in Fig. 2 c, the 8-4-1-1-1-1 solution undergoes a torus bifurcation, whereby a third frequency is added to the dynamics, while all clusters stay intact. The resultant three-frequency motion is resistant to the addition of small random numbers over a nonzero c_2 interval. This is notable as stable quasiperiodic dynamics with more than two frequencies is usually not observed.

It has even been proven that quasiperiodic dynamics with three or more frequencies are in general structurally unstable^{1,29}. However, such stable quasi-periodic motion on T^3 has also been observed in Stuart-Landau oscillators with linear global coupling²⁰ and could be due to the rotational invariance of the differential equations.

If we initialize the 8-4-4 solution at $c_2 = -0.71$ and $\eta = 0.63$ and slowly increase c_2 along the horizontal black line in Fig. 2 c, the maxima of $\text{Re}(w_k)$ for $k = 1, \dots, 16$ develop as in Fig. 3 a: Initially, there are one maximum of the oscillators in the cluster of eight (blue) and two shared maxima of the two period-2 clusters of four (red). When one of these clusters splits up into two smaller clusters of two at the period-doubling bifurcation PD₂, the maxima of these smaller clusters henceforth appear as four distinct yellow lines. In the next period-doubling bifurcation (PD₃), these lines split up into eight.

From the fully synchronized solution to the 8-4-(4×1)

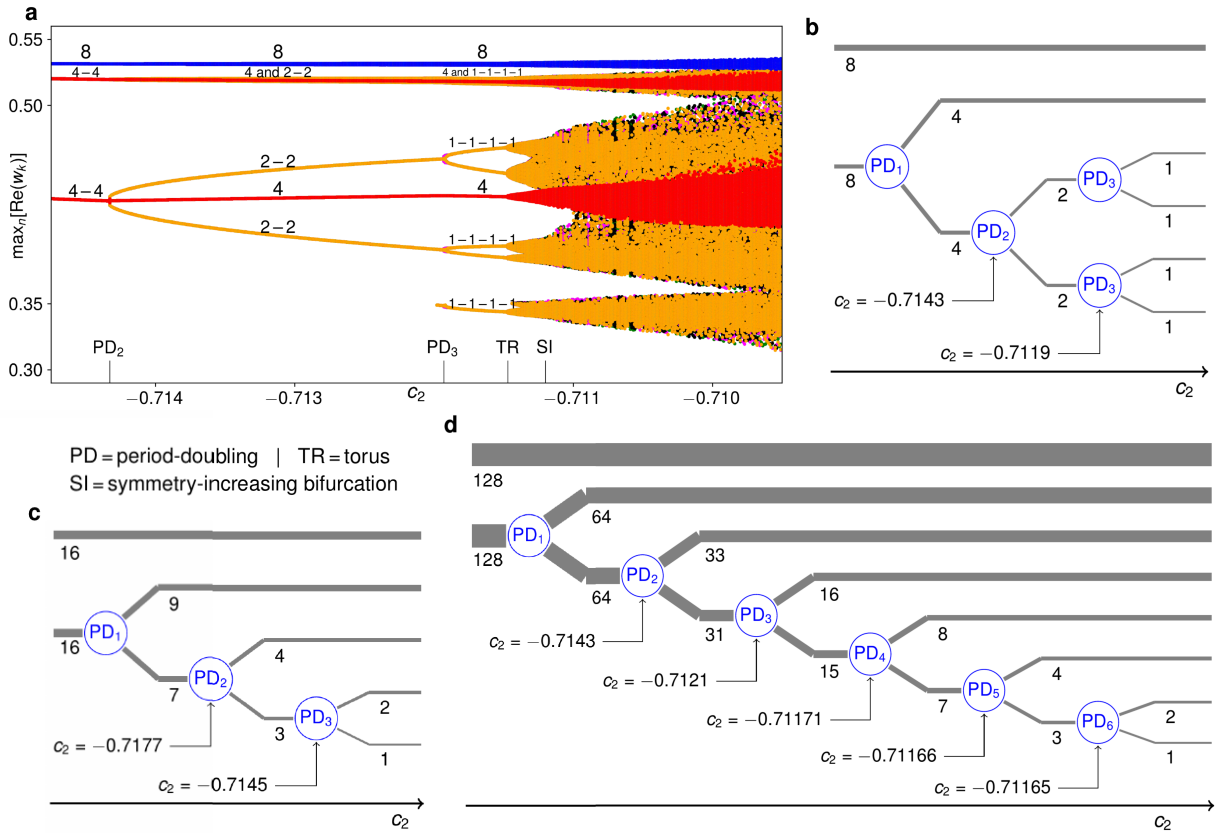


FIG. 3. **Cluster-splitting cascades for different N .** **a** Maxima of $\text{Re}(w_k)$ in an $N = 16$ c_2 -incremented simulation at $\eta = 0.63$. Labels on the figure mark the clusters reaching the different maxima as the solution changes from 8-4-4 via 8-4-2-2 to 8-4-(4 \times 1). Labels on the abscissa mark occurring bifurcations. The additional smallest yellow maximum appearing at $c_2 \approx -0.712$ is caused by the continuous deformation of the oscillator trajectories and not by a bifurcation. At $c_2 \approx -0.7115$, the torus bifurcation to three-frequency dynamics manifests itself in a distinct broadening of the formerly discrete maxima. **b** Schematic portrayal of the period-doubling cluster splittings in the simulation in **a**. **c-d** Like **b** for c_2 -incremented simulations at $\eta = 0.63$ with $N = 32$ and $N = 256$, respectively, based on quantitative results in Supplementary Figures 1-3.

solution, four discrete steps of symmetry breaking have taken place: one initial equivariant Hopf bifurcation, as well as three equivariant period-doubling bifurcations. The three last of these steps are shown schematically in Fig. 3 b. Similar stepwise symmetry-breaking is observed both for larger N and when the smallest cluster does not break up into equal-sized parts (Fig. 3 c). The larger N is, the more steps occur, at ever closer parameter values, and for $N = 256$, as many as seven steps can be observed (see Fig. 3 d). The $N/2$ - $N/2$ two-cluster solution thus gives rise to a cluster-splitting cascade, producing a multitude of coexisting multi-cluster states and, most notably, hierarchical clustering.

Symmetry-increasing bifurcation and temporary clusters

At the end of a cascade of cluster-splitting period-doubling bifurcations, a torus bifurcation usually occurs (see e.g. the red bifurcation line in Fig. 2 c). The result-

tant T^3 motion is usually stable for a nonzero parameter interval, before being superseded by less regular dynamics in a *symmetry-increasing bifurcation*³⁰, wherein several distinct, but equivalent variants of the same solution collide. These variants exist because equation (1) is \mathbb{S}_N -equivariant. Thus, any solution remains a solution when any of the oscillators are interchanged, and each solution (except the fully synchronized one) exists in the form of several distinct symmetric variants in phase space. (For example, if we interchange an oscillator from the blue cluster in Fig. 1 a with one from the red, the outcome is such a different, but equivalent variant.)

All solutions investigated here are at least periodic in the co-rotating frame. The attractor corresponding to a stable solution thus occupies more than a single point in the phase space spanned by w_k , $k = 1, \dots, N$. As these attractors become more complex, and especially as the aforementioned torus bifurcation renders the motion quasiperiodic, the part of phase space they occupy increases in extent. This of course applies equally to all the

symmetrized variants of each solution.

At some point, two or more variants might grow to touch each other in phase space. When this happens, the variants involved in the collision merge to become a single instance of a new solution, of which there are fewer distinct mirror-image variants in total. The attractor on which the new solution lives is correspondingly more symmetric than the attractors of the colliding variants. One symmetry-increasing bifurcation can in general be followed by another, further increasing the attractor symmetry.

In the $N = 16$ case in Fig. 3a, the first symmetry-increasing bifurcation only disrupts the former rigid cyclic order of the four single oscillators, inherited from the solution in Fig. 2e-f (i.e., that the purple oscillator trails the yellow one, which trails the pink, and so on). In other cases, some of the intact clusters of a certain colliding variant contain oscillators that are in a different cluster in some of the other variants this variant is colliding with. Then, the symmetry-increasing bifurcation destroys these clusters. Such a scenario is schematically shown in Fig. 4: In this $N = 8$ example of two colliding 4–2–1–1 variants, the cluster of two in one of the variants contains oscillators 5 and 6, while in the other, it contains oscillators 5 and 7. Because the two variants are identical mirror-images of each other, they must both be treated equally by the collision. Thus, the oscillators 5 and 6, which are clustered in only one of the variants, cannot remain together after the collision, nor can the oscillators 5 and 7. The result is thus a 4–1–1–1 state in which all four single oscillators behave identically.

Similarly for larger ensembles, as the attractor symmetry is increased, the number of single oscillators, in general, grows, in a sense also decreasing the overall order of the ensemble.

The $N = 32$ cluster-splitting cascade in Fig. 3c is also followed by symmetry-increasing bifurcations, and at some point, the long-term cluster-size distribution becomes $16-9-(7 \times 1)$. A time series of the resulting solution is shown in Fig. 5a: Here, the seven single oscillators in yellow move similarly to the clusters of four, two and one in the former $16-9-4-2-1$ solution, being close to deep minima when the red cluster of nine is at a shallow minimum and vice versa. They also repeatedly congregate into loose temporary agglomerations of four, three and two oscillators, respectively. This is further illustrated by Fig. 5b-d, where the cross-correlation between all oscillator trajectories is calculated every 10^4 time steps. Two oscillators are said to be in the same cluster if their cross-correlation is greater than $1 - \varepsilon$ for $\varepsilon = 10^{-8}$ (b), $\varepsilon = 10^{-4}$ (c) or $\varepsilon = 10^{-2}$ (d). Sometimes, a temporary cluster of three detected for a certain ε becomes a cluster of four for larger values of ε , such as the blue cluster at $t = 7 \cdot 10^4$ and the red cluster at $t = 1.2 \cdot 10^5$. This means that four oscillators are loosely congregating here, but that three of the oscillators are more strongly clustering than the fourth. The ensemble is thus less closely approaching the remains of a formerly stable $16-9-4-2-1$ attractor

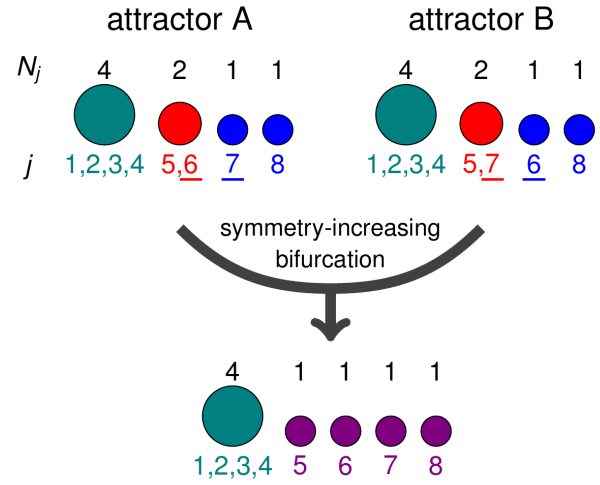


FIG. 4. **Schematic of a symmetry-increasing bifurcation destroying clusters.** Here, two equivalent variants of a 4–2–1–1 solution collide. The increase in attractor symmetry caused by the collision implies that any two oscillators which behaved equivalently in either of the variants must also behave equivalently in the resulting solution. Because the cluster of two contains different oscillators in the two variants, this cluster is necessarily destroyed.

in phase space.

Dynamics like those in Fig. 5 have previously been observed by Kaneko in globally coupled logistic maps when the phase space becomes so full of mirror-image attractors that they inevitably intrude upon each other³¹. The outcome is a form of *chaotic itinerancy*³², wherein the system meanders between the *attractor ruins* of previous attractors, each of them relatively low-dimensional, but connected by higher-dimensional transitional motion¹⁵.

Also found in globally coupled maps is *precision-dependent clustering*, wherein trajectories of individual maps that are unclustered when distinguished with high precision appear to repeatedly merge into the ever thicker branches of a clustering tree when the precision is decreased¹⁴. In our ensemble, this occurs as a consequence of the symmetry-breaking period-doubling cascade. For example, past the $N = 256$ cascade in Fig. 3 (at $c_2 \approx -0.71162$), we encounter a $128-64-33-(31 \times 1)$ itinerant solution that for small $\varepsilon \leq 10^{-5}$ is found to have an additional cluster of usually 16, sometimes 18 or 19 oscillators, while the remaining oscillators repeatedly form ephemeral smaller clusters of strongly fluctuating sizes. For $\varepsilon = 10^{-4}$, a cluster of size 15 is also sometimes detected (along with that of 16), and for $\varepsilon = 10^{-3}$ the sizes are always $128-64-33-16-15$, $128-64-33-18-13$ or $128-64-33-19-12$. For $\varepsilon = 10^{-2}$, they are $128-64-33-31$ throughout, and for $\varepsilon = 10^{-1}$, $128-64-64$. The same pattern to some extent already applies in the quasiperiodic domain of Fig. 3b-d, where clusters are most strongly correlated with those other clusters from which they most

recently split.

If we initialize the ensemble in the itinerant state beyond a symmetry-increasing bifurcation and gradually change the parameters back towards more regular motion, the transition to the relevant two-cluster solution will simply be the reverse of the one that created the itinerant state. For example, if we initialized the $N = 16$ ensemble in the state at the right edge of Fig. 3a and slowly decreased c_2 , this would produce the same sequence of bifurcations. See Supplementary Fig. 4.

When the equation parameters are incremented too far into the regime of chaotic itinerancy, the ensemble will often jump to an entirely different solution. Beyond the

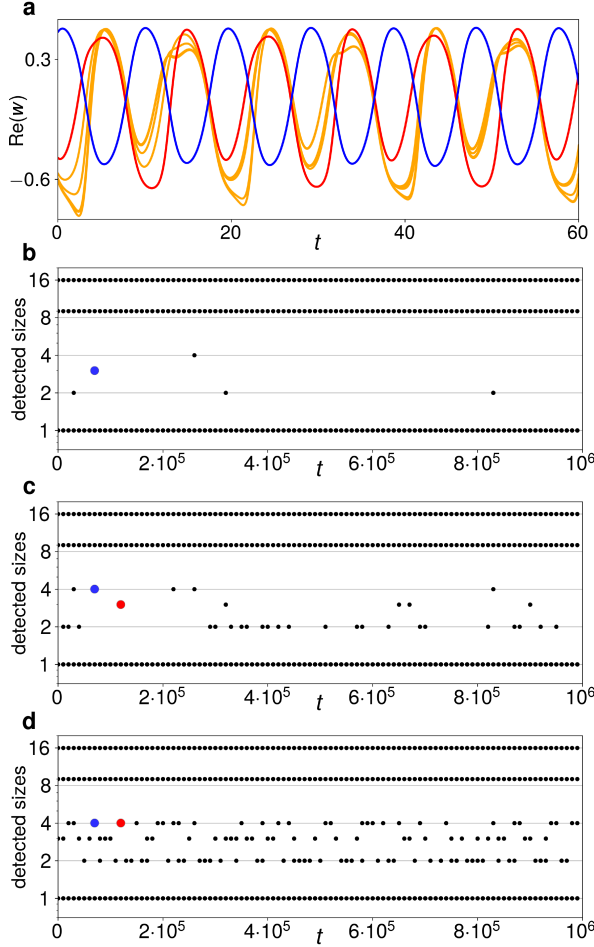


FIG. 5. **Partially clustered 16-9-(7x1) solution past the cascade in Fig. 3c.** **a** Time series of $\text{Re}(w_k)$ for $c_2 = -0.712$ and $\eta = 0.63$. The single oscillators (yellow) reach a deep minimum approximately when the cluster of nine (red) reaches a shallow minimum and the cluster of 16 a maximum. **b-d** Cluster sizes detected when two oscillators are said to be clustered if their cross-correlation over an interval of 800 time units is $> 1 - \varepsilon$ for $\varepsilon = 10^{-8}$, 10^{-4} and 10^{-2} , respectively. The large red and blue dots mark two exemplary loose oscillator conglomerations at different sensitivities ε .

16-9-7-derived state in Fig. 5, it e.g. jumps to the blue hitherto co-stable 16-8-8-derived branch. However, the end result can also be the destruction of all permanent clusters and the motion of only single oscillators on a fully symmetric chaotic attractor. See Supplementary Figures 5-7.

Emergence of a chimera state

In our context, a chimera state is an $N_1 - ((N - N_1) \times 1)$ solution. The modulated-amplitude chimeras previously found in equation (1) have significantly more synchronized (N_1) than unsynchronized ($N - N_1$) oscillators³³. This suggests they have not evolved from balanced two-cluster solutions like the ones studied above. Yet, our above results can be used to explain how they are created. If we e.g. initialize an $N = 20$ ensemble as an $3N/4 - N/4 = 15 - 5$ solution (Fig. 6a) for $c_2 = -0.87$ and $\eta = 0.67$, the bifurcation diagram in Fig. 1k tells us it will undergo a cluster-splitting period-doubling bifurcation if c_2 is increased. The resulting 15-3-2 period-2 solution is shown in Fig. 6b. Further up in c_2 , the cluster of two is split into single oscillators (Fig. 6c). Then, a torus bifurcation smears the previously closed trajectories into continuous bands (Fig. 6d).

Finally, the current 15-3-1-1 variant collides with nine others in a symmetry-increasing bifurcation. This destroys the cluster of three, resulting in a 15-(5x1) chimera state (Fig. 6e). Note how the three oscillators that are temporarily close to each other in Fig. 6e (red, yellow, grey, in the lower left) are not all the same three that were clustered in Figs. 6b-d (red, purple, grey). The ensemble is currently close to the ruin of a different 15-3-1-1 solution variant, and the chimera state is thus also an example of chaotic itinerancy. For $N = 200$, the transition from a 150-50 to a 150-(50x1) solution proceeds along a much more involved, but essentially similar path. See Supplementary Figure 8.

Generality of results I – pitchfork maps

Other theoretical \mathbb{S}_N -symmetric systems can also develop as discussed in the previous sections. One such system is the following ensemble of N globally coupled time-discrete maps:

$$y_k(n+1) = (1 + \alpha - |y_k(n)|^2) \cdot y_k(n) - \frac{1}{N} \sum_{j=1}^N (\alpha - |y_j(n)|^2) \cdot y_j(n), \quad (4)$$

where $y_k(n) \in \mathbb{R}$ denotes the n th iteration of the k th map, $k = 1, \dots, N$, and α is a real-valued parameter. Each map $y_k(n+1) = (1 + \alpha - |y_k(n)|^2) \cdot y_k(n)$ (without the coupling) is modeled on the normal form of the supercritical pitchfork bifurcation²⁶, $x_{n+1} = x_n + \mu x_n - x_n^3$

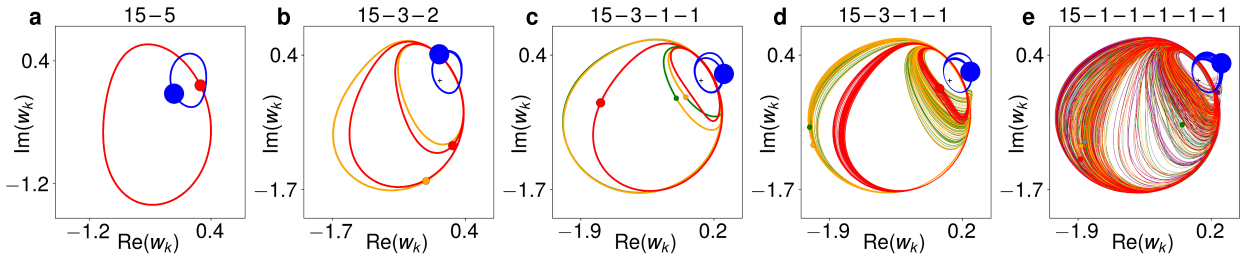


FIG. 6. **Steps from 15-5 two-cluster solution to chimera state.** $N = 20$, $\nu = 0.1$ and $\eta = 0.67$, proceeding along the black line in Fig. 1 e. **a** 15-5 solution for $c_2 = -0.87$. **b** 15-3-2 period-2 solution for $c_2 = -0.82$. **c** 15-3-1-1 period-4 solution for $c_2 = -0.725$. The two largest loops of the two single oscillators are almost equal. **d** 15-3-1-1 three-frequency solution for $c_2 = -0.71$. **e** 15-(5 \times 1) chimera at $c_2 = -0.705$, after collision of mirror-image attractors.

Altogether, the system (4) is subject to a conservation law:

$$\langle y(n+1) \rangle = \frac{1}{N} \sum_{k=1}^N y_k(n+1) = \langle y(n) \rangle, \quad (5)$$

that is, the ensemble average $\langle y(n) \rangle = \langle y(0) \rangle \forall n \in \mathbb{N}$ remains constant independent of the individual map behaviour and thus effectively constitutes an additional parameter $\beta = N^{-1} \sum_k y_k(0)$, implicitly set by choosing the initial value of each map $y_k(0)$.

For suitable values of α and β , equation (4) has stable period-1 (i.e., constant) two-cluster solutions, among them a balanced $N/2 - N/2$ solution for any even N . As an example, for $\alpha = 0.7$ and $\beta = 0.15$ this solution is given by $y_k(n) \approx -0.645$ for $k = 1, \dots, N/2$ and $y_k(n) \approx 0.945$ for $k = N/2 + 1, \dots, N$. (Of course, any other $N/2$ of the N maps could also be in the first cluster; that would simply constitute a different equivalent variant of the same solution.) Clearly, the ensemble average remains constantly equal to $\beta = 0.15$.

Let us now again consider the concrete case $N = 16$. If α is slowly increased, the $N/2 - N/2 = 8 - 8$ solution undergoes an equivariant period-doubling bifurcation at $\alpha = 0.708$. Like in the Stuart-Landau ensemble, several three-cluster period-2 solutions emerge, one of which is the $N/2 - N/4 - N/4 = 8 - 4 - 4$ solution in Fig. 7 a. For a further increase of α , this solution also undergoes a period-doubling bifurcation, wherein *both* clusters of four are split into a total of four period-4 clusters of two, as seen in Fig. 7 b. The cluster of eight (at $y_k(n) \approx -0.7$) still remains period-1, but has been left out of the figure for a better view. This sequence of two cluster splittings, summarized in Fig. 8 a, is strongly reminiscent of the two last steps in Fig. 3 b.

For sufficiently large ensemble sizes N , when the $N/2 - N/2$ solution is destabilized in its period-doubling bifurcation, several of the resultant three-cluster solutions emerge as co-stable. For $N = 128$ and $\beta = 0.15$, one of the stable solutions is a 64-33-31 period-2 solution whose trajectory looks more or less like that of the $N/2 - N/4 - N/4$ solution in Fig. 7 a. (The maxima of the period-2 trajectory of the cluster of 33 are only slightly smaller than

those of the cluster of 31, and its minima slightly less deep, in order to fulfill the condition $\langle y(n) \rangle = \beta \forall n$.) When α is gradually increased for this 64-33-31 solution, an equivariant period-doubling also occurs, but here, only the cluster of 31 is split. The result is the 64-33-16-15 period-4 solution shown in Fig. 7 c. (Here, the cluster of 64 also moves with a small period-4 component, due to the asymmetry in the smaller clusters.) If α is increased somewhat further, it results in the 64-33-16-8-7 period-8 solution in Fig. 7 d. Even further upward in α , two more cluster-splitting period-doubling bifurcations occur, resulting in the overall sequence of cluster sizes shown in Fig. 8 b. Thus, equation (4) undergoes a cluster-splitting cascade remarkably similar to that of equation (1).

The coupled maps of equation (4) also exhibit transitions likely to be symmetry-increasing bifurcations. Past the α interval covered in Fig. 8 b, the $N = 128$ ensemble namely also enters several consecutive α intervals wherein the sizes of only some clusters remain stable for several α increments. Other clusters seemingly appear and disappear erratically, as already observed for the Stuart-Landau ensemble in Fig. 5. We even encounter 64-(64 \times 1) chimera states, as shown in Supplementary Figure 10.

The difference between the two systems (1) and (4) lies in the details. For example, we have already seen that in the Stuart-Landau ensemble, the period-doubling bifurcation of the $N/2 - N/4 - N/4$ solution produces a stable $N/2 - N/4 - N/8 - N/8$ solution, whereas the analogous bifurcation in the coupled maps gives rise to a stable $N/2 - (4 \times N/8)$ solution (comparing Fig. 3 b and Fig. 8 a). Another difference can be observed if we track the 128-65-63 period-2 solution to equation (4) for $N = 256$ upward in α for $\beta = 0.15$. At first, it will give rise to a stable 128-65-32-31 period-4 solution. However, the next bifurcation encountered will not be another period-doubling, but an equivariant pitchfork splitting the cluster of 65. Thus, the pattern of stepwise cluster splitting, whereby always the smallest cluster is the next one to be split, as observed in both Figs. 3 c-d and 8 b, ends prematurely. In this case, no more discrete cluster splittings occur and the next qualitative change of the dynamics is a symmetry-increasing bifurcation, as

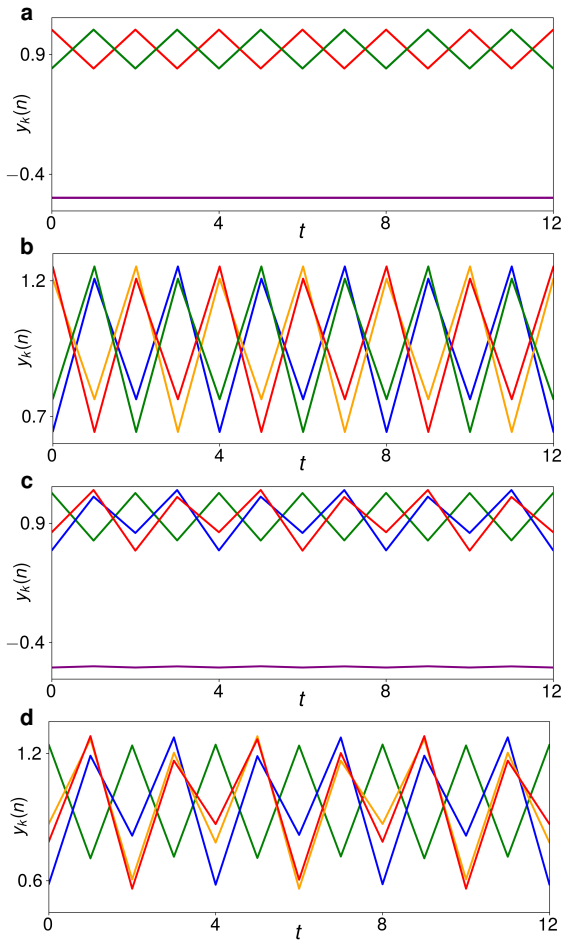


FIG. 7. **Trajectories of time-discrete maps.** **a** 8–4–4 solution for $N = 16$, $\alpha = 0.8$ and $\beta = 0.15$, wherein the clusters of 4 are period-2 and the cluster of 8 is constant. **b** 8–(4×2) solution emerging in a period-doubling of the solution in **a**, with the cluster of 8 not shown for better resolution. $\alpha = 0.86$. **c** 64–33–16–15 period-4 solution for $N = 128$, $\alpha = 0.86$ and $\beta = 0.15$. Cluster trajectories: 64 purple, 33 green, 16 blue, 15 red. **d** 64–33–16–8–7 period-8 solution emerging in a period-doubling of the solution in **c**, with the cluster of 64 not shown. $\alpha = 0.87$. The cluster of 15 has split into smaller clusters of 8 (red) and 7 (yellow).

seen in Supplementary Figure 11.

Generality of results II – electrochemical experiments

As stated in the introduction, equation (1) is inspired by electrochemical experiments. In fact, the theoretical model was originally more complicated, consisting not of discrete identical oscillators, but of a continuous oscillatory medium coupled via both global and local (diffusional) coupling^{17,34}. Later results showed that most of the qualitative dynamics obtained in this extended model could still be reproduced if the diffusion was set

to zero³³, thus paving the way for our purely globally coupled ensemble. Meanwhile, the experimental system itself has been found to exhibit a vast amount of dynamical phenomena^{17,34–41}. Below, we revisit four different spatiotemporal states representative of solutions in the transition scenario outlined above.

The central component of the experiment is an n-type silicon (Si) electrode, immersed in a fluoride-containing electrolyte. A voltage is applied across the electrode, which is also illuminated with a laser. Thus, an oxide layer is grown photo-electrochemically on the Si surface. Simultaneously, the fluoride species in the electrolyte etches away the silicon oxide in a purely chemical process⁴². An ellipsometric setup is used to measure the spatiotemporal changes in the optical pathway through the Si|SiO₂|electrolyte interface^{34,35,43}.

For a wide range of experimental parameters, the ellipsometric signal can be made to oscillate homogeneously with a simple period. If the parameters are suitably changed, the electrode undergoes a period-doubling bifurcation, resulting in two anti-phase clusters connected by a mediating region with rather low amplitude. An exemplary snapshot of the electrode in this state is shown in Fig. 9a, together with the time series of a section. The location of the section is indicated by the blue line on the image of the electrode. In the depicted snapshot, a rather high ellipsometric signal, displayed by the red color in the upper part of the electrode, coexists with a rather low signal in the lower right, displayed by the blue color. In the time series below, we recognize the oscillation of the ellipsometric signal; the two regions, connected by the cut, oscillate with the same frequency, but in anti-phase to each other. Note that the global time series exhibits a simple periodic oscillation, which, as demonstrated in Supplementary Fig. 12, defines a rotating frame. Thus, as in the above simulation results, the experimental results are depicted in a rotating frame, that is, the spatial mean of each frame has been subtracted from every point in the same frame.

Fig 9b shows the same electrode after a further parameter variation (see appendix). This time, in order to properly view the spatiotemporal development, the spatial coordinate of the time series is composed of two lines forming an angle. Clearly, the variation of the parameters has resulted in a period doubling-bifurcation affecting the right and left side of the electrode, corresponding to the upper and lower part of the time-series spatial coordinate. These regions now oscillate with double the period of the oscillations in the upper part of the electrode and are in anti-phase with respect to each other.

In Fig. 9c, a deep blue region can be seen on the right of the electrode snapshot. This region appears rather regular throughout whereas the rest of the electrode is irregularly patterned. In the time series of the spatial cut, the deep blue area appears in the lower quarter. It is indeed found to exhibit simply periodic oscillations, whereas most of the electrode is turbulent. This solution is a chimera state.

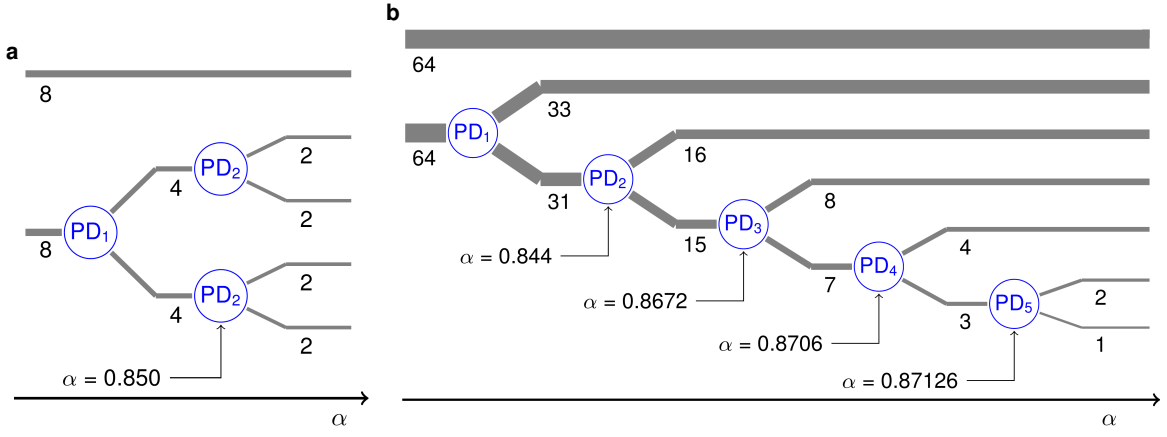


FIG. 8. **Cluster splitting in the time-discrete maps.** **a** Schematic portrayal of the period-doubling cluster splittings as α is increased for $\beta = 0.15$ and an initial 8–8 solution. **b** Like **a** for a possible cluster-splitting cascade for $N = 128$ and $\beta = 0.15$. The schematics are based on the quantitative results in Supplementary Figures 9 and 10, respectively.

Finally, Fig. 9d depicts a state that is turbulent throughout. Here, irregular patterns arise over the entire electrode. The time series shows that the spatial incoherence is accompanied by aperiodic behaviour.

Note that the measurements in Fig. 9a and b were carried out on a different day and with a different electrolyte than the ones in Fig. 9c and d. The electrolyte composition seems to be a crucial parameter for some of the presented states, yet it is a parameter which cannot be easily varied during a measurement day. Spatially homogeneous oscillations can, however, be found with both of the electrolytes used here.

DISCUSSION

In this article, we have shown how a globally coupled system can transition from full symmetry to ever more complex coexistence patterns through a sequence of discrete symmetry-breaking steps. The transition begins with a cascade of cluster-splitting bifurcations, and at each step of this cascade, either one cluster or two similarly behaving clusters are split into smaller clusters. In an ideal form of the cascade, the next cluster to split is always the smallest one, ultimately creating a multi-cluster state with very different cluster sizes, wherein the smallest “cluster” is just a single oscillator. This ideal cascade is schematically depicted in the left part of Fig. 10.

The cluster-splitting cascade is followed by one or more symmetry-increasing bifurcations, breaking ever more clusters up into single oscillators. Even though they destroy clusters, these bifurcations are symmetry-increasing because the single oscillators they produce all behave equally for $t \rightarrow \infty$. Thus, the attractor is symmetric with regards to the interchange of any two of these oscillators.

In practice, the symmetry-increasing transition is often

cut short by interactions with other solution branches and the ensemble at some point is thrown onto a different, hitherto co-stable solution. In the ideal case when it is allowed to continue sufficiently long, the end result is ultimately a turbulent state of only single oscillators, all behaving equally in the long run. A chimera state is then the last step but one in the cascade.

Our primary model has been one of $N = 2^n$, $n \in \mathbb{N}$ Stuart-Landau oscillators with nonlinear global coupling and our main focus on the case where the fully synchronized solution is initially split into two equal clusters $N/2 - N/2$. However, the cluster-splitting cascade is also observed for less balanced initial states, such as the 15–5 solution which transitions via 15–3–2 to 15–3–1–1 in Fig. 6. The cascade is also not dependent on the choice of $N = 2^n$, but similarly occurs for odd N as well, as shown in Supplementary Figure 13. Nor is it conditional upon the particular chosen model, but can be similarly observed in globally coupled time-discrete maps.

Symmetry-increasing bifurcations also occur whether the cluster-size distribution of the initial two-cluster state emerging from synchrony is $N_1/N_2 = 1$ (Fig. 3a) or $N_1/N_2 = 3$ (Fig. 6). Moreover, it is observed in both the Stuart-Landau oscillators (1) and the pitchfork maps (4). The general outcome of a symmetry-increasing bifurcation, chaotic itinerancy, has previously been found in globally coupled logistic maps, along with both multi-cluster states, chimeras and precision-dependent clustering, but without an overall explanation of how these phenomena might be bifurcation-theoretically related to each other^{14,15,31,32}. This suggests that the bifurcation scenario uncovered here occurs in those logistic maps as well.

What are the prerequisites for the observed bifurcation scenario? The high permutation symmetry of globally coupled equations is probably a central factor shared by the Stuart-Landau oscillators and the pitchfork maps (and Kaneko’s logistic maps). \mathbb{S}_N not only has many subgroups,

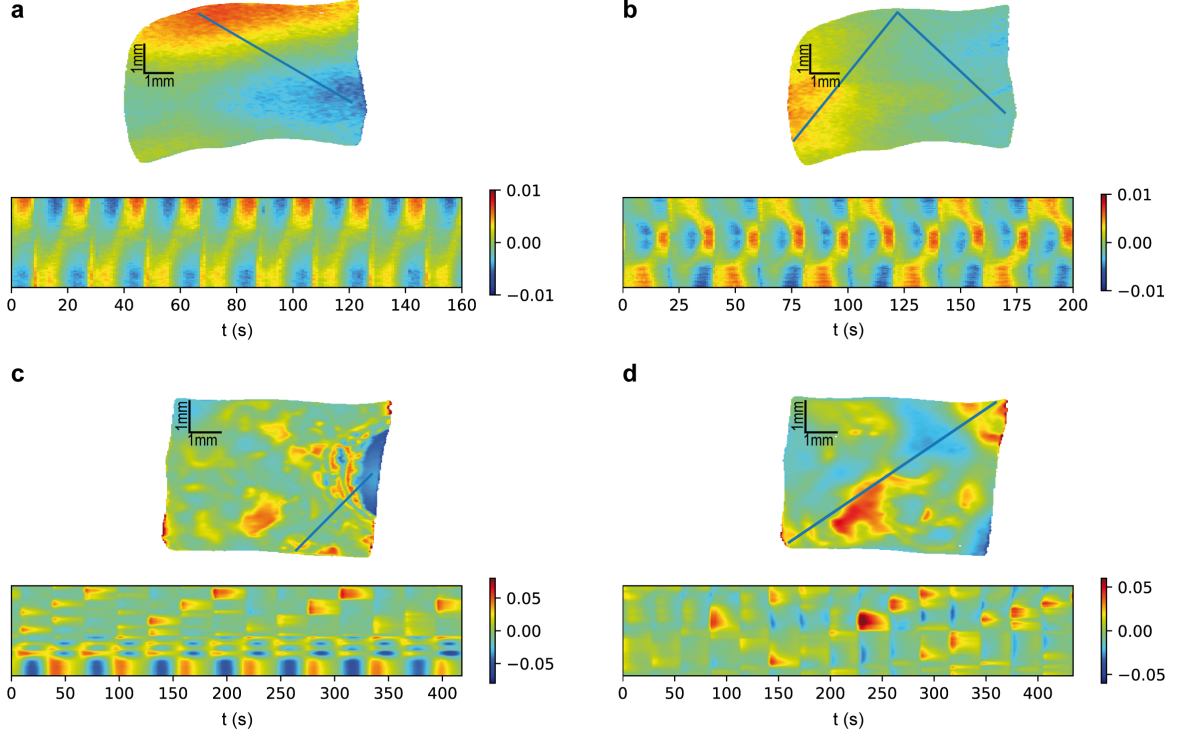


FIG. 9. **Ellipsometric measurements of four different experimental states.** Each state shows a snapshot of the electrode and the time-series along a section on the electrode as indicated by the blue lines in the electrode snapshots. Note that the dynamics are shown in a frame rotating, where the uniform oscillation of the spatial average has been subtracted. **a** anti-phase two-cluster state, **b** subharmonic cluster state, **c** chimera state and **d** turbulent state. The size of the electrode in **a** and **b** is $6.0\text{ mm} \times 4.3\text{ mm}$ (width \times height), while in **c** and **d** it is $5.8\text{ mm} \times 4.6\text{ mm}$. For parameter values and experimental details, see the Methods section.

but most of these subgroups have many subgroups as well, and so on. This intricate subgroup structure is mirrored in the hierarchy of successively less symmetric quasiperiodic solutions. Moreover, because \mathbb{S}_N is much larger than those of its subgroups corresponding to the more intricate solutions, there are many mirror-image variants of the latter, causing the symmetry-increasing bifurcations and the itinerant coexistence patterns that these produce.

The nonlinear nature of the global coupling could be another relevant system property, and all three systems studied here are coupled nonlinearly (as are Kaneko's logistic maps). However, symmetry-increasing bifurcations have also been observed in Stuart-Landau oscillators with linear global coupling⁴⁴, for an ensemble size as small as $N = 4$. Such an ensemble is of course too small to exhibit an evident cluster-halving cascade, and instead, the symmetry-increasing bifurcation was preceded by a non-equivariant Feigenbaum period-doubling cascade to chaos. To test whether our full bifurcation scenario can occur for linear global coupling as well, is thus an exciting task for future studies.

In the case of the Stuart-Landau oscillators, an ad-

ditional factor required by the cluster-splitting cascade is the amplitude variation of the cluster orbits. If the clusters were to have fixed amplitudes, i.e., $d|w_k|/dt = 0$ for all oscillators w_k , then there could namely only be three different cluster, due to the Stuart-Landau oscillator being a third-order polynomial⁴⁵. This would render any extended cluster-splitting impossible. On the other hand, the fact that cluster-splitting takes place by means of period-doubling seems to imply that the amplitudes must vary over the course of a full oscillation period.

What all discussed symmetry-increasing bifurcations seem to require, is a certain dimensionality of the dynamics before the bifurcation. (That is, trajectories can for example not be zero-dimensional fixed points or one-dimensional periodic orbits.) In the Stuart-Landau ensemble with nonlinear global coupling and in the pitchfork maps, this extra dimensionality arises in the torus bifurcation at the end of the cluster-splitting cascade. In the aforementioned Stuart-Landau oscillators with linear global coupling, it is provided by a period-doubling cascade to chaos, and in the globally coupled logistic maps, the maps are also in the chaotic regime.

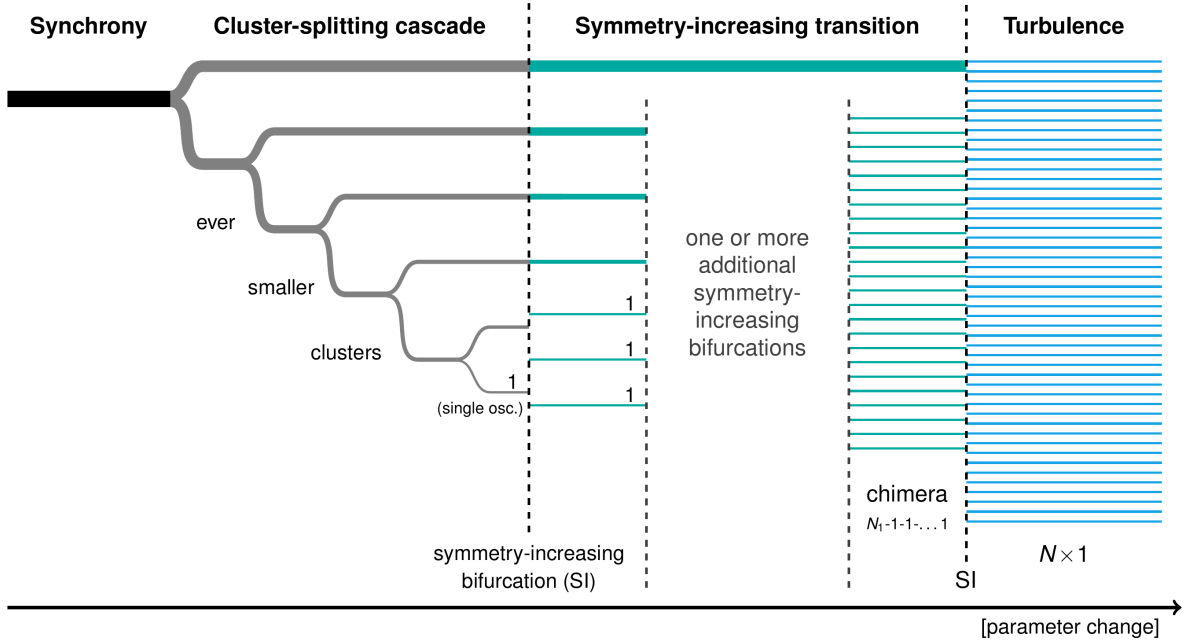


FIG. 10. **Ideal transition from synchrony to turbulence.** The synchronized state is initially broken into two clusters. These clusters are in turn split into successively smaller clusters in a cluster-splitting cascade. When the smallest cluster is just a single oscillator, a symmetry-increasing bifurcation occurs. Hereby, one or more clusters are abruptly broken into single oscillators that henceforth all behave equally in the long run. Additional symmetry-increasing bifurcations ultimately lead to a turbulent state of only single oscillators. The last step but one is often a chimera state.

Finally, we again consider the experiments. These exhibit a series of patterns which are similar to the ones in the simulations. The anti-phase clusters in Fig. 9a emerge from the homogeneous oscillation and bring about a second frequency. Fig. 9b and c exhibit coexistence patterns, consisting either of clusters of different frequencies (b) or of the coexistence of a regularly oscillating region and irregular motion (c). Fig. 9d is a completely turbulent state. These states are clearly reminiscent of the ones found in the simulations, and we are not aware of other bifurcation scenarios that include these states.

Nevertheless, the connection between the experiments and the discussed bifurcation scenario has yet to be clearly demonstrated. As mentioned above, one difficulty is that the electrolyte composition, which is difficult to change within the same experiment, seems to be a crucial bifurcation parameter. Despite the prior equivalence of many results with and without diffusion, the diffusive coupling on the electrode could also potentially influence the dynamical transition. This could for example be investigated in experiments with amorphous instead of crystalline silicon. Altogether, many effects of different parameters on the dynamics are only poorly understood and the detailed oscillation mechanism is still unknown. There is thus great potential for further studies in this direction. The same applies to the search for other experimental systems

that exhibit the discussed transition from synchrony to turbulence.

REFERENCES

- ¹Argyris, J. H., Faust, G., Haase, M. & Friedrich, R. *An Exploration of Dynamical Systems and Chaos*, (Springer Berlin Heidelberg, Berlin, Heidelberg2015).
- ²Cross, M. C. & Hohenberg, P. C. Pattern formation outside of equilibrium. *Rev. Mod. Phys.* **65**, 851–1112 (1993).
- ³Cross, M. C. & Hohenberg, P. C. Spatiotemporal Chaos. *Science* (80-.). **263**, 1569–1570 (1994).
- ⁴Nelkin, M. In What Sense Is Turbulence an Unsolved Problem? *Science* (80-.). **255**, 566–570 (1992).
- ⁵Warhaft, Z. Turbulence in nature and in the laboratory. *Proc. Natl. Acad. Sci.* **99**, 2481–2486 (2002).
- ⁶Strogatz, S. H. From Kuramoto to Crawford: Exploring the onset of synchronization in populations of coupled oscillators. *Phys. D Nonlinear Phenom.* **143**, 1–20 (2000).
- ⁷Pikovsky, A., Rosenblum, M. & Kurths, J. *Synchronization*. Cambridge Nonlinear Science Series, (Cambridge University Press2001).
- ⁸Kuramoto, Y. & Battogtokh, D. Coexistence of Coherence and Incoherence in Nonlocally Coupled Phase Oscillators. *Nonlinear Phenom. Complex Syst.* **5**, 380–385 (2002).
- ⁹Abrams, D. M. & Strogatz, S. H. Chimera states for coupled oscillators. *Phys. Rev. Lett.* **93**, 174102 (2004).
- ¹⁰Panaggio, M. J. & Abrams, D. M. Chimera states: Coexistence

- of coherence and incoherence in networks of coupled oscillators. *Nonlinearity* **28**, R67–R87 (2015).
- ¹¹Schöll, E. Synchronization patterns and chimera states in complex networks: Interplay of topology and dynamics. *Eur. Phys. J. Spec. Top.* **225**, 891–919 (2016).
 - ¹²Omel'chenko, O. E. The mathematics behind chimera states. *Nonlinearity* **31**, R121–R164 (2018).
 - ¹³Omel'chenko, O. E., Maistrenko, Y. L. & Tass, P. A. Chimera states: The natural link between coherence and incoherence. *Phys. Rev. Lett.* **100**, 044105 (2008).
 - ¹⁴Kaneko, K. Clustering, coding, switching, hierarchical ordering, and control in a network of chaotic elements. *Phys. D Nonlinear Phenom.* **41**, 137–172 (1990).
 - ¹⁵Kaneko, K. From globally coupled maps to complex-systems biology. *Chaos* **25**, 097608 (2015).
 - ¹⁶Wiesenfeld, K. & Hadley, P. Attractor crowding in oscillator arrays. *Phys. Rev. Lett.* **62**, 1335–1338 (1989).
 - ¹⁷Schmidt, L., Schönleber, K., Krischer, K. & García-Morales, V. Coexistence of synchrony and incoherence in oscillatory media under nonlinear global coupling. *Chaos* **24**, 013102 (2014).
 - ¹⁸Kuramoto, Y. *Chemical Oscillations, Waves, and Turbulence*, vol. 19 of *Springer Series in Synergetics*, (Springer Berlin Heidelberg, Berlin, Heidelberg 1984).
 - ¹⁹Hakim, V. & Rappel, W. J. Dynamics of the globally coupled complex Ginzburg-Landau equation. *Phys. Rev. A* **46**, R7347–R7350 (1992).
 - ²⁰Nakagawa, N. & Kuramoto, Y. Collective Chaos in a Population of Globally Coupled Oscillators. *Prog. Theor. Phys.* **89**, 313–323 (1993).
 - ²¹Sethia, G. C. & Sen, A. Chimera states: The existence criteria revisited. *Phys. Rev. Lett.* **112**, 144101 (2014).
 - ²²Ku, W. L., Girvan, M. & Ott, E. Dynamical transitions in large systems of mean field-coupled Landau-Stuart oscillators: Extensive chaos and cluster states. *Chaos* **25**, 123122 (2015).
 - ²³Kemeth, F. P., Haugland, S. W. & Krischer, K. Cluster singularity: The unfolding of clustering behavior in globally coupled Stuart-Landau oscillators. *Chaos* **29**, 023107 (2019).
 - ²⁴Schmidt, L. & Krischer, K. Clustering as a prerequisite for chimera states in globally coupled systems. *Phys. Rev. Lett.* **114**, 034101 (2015).
 - ²⁵Moehlis, J. & Knobloch, E. Equivariant dynamical systems. *Scholarpedia* **2**, 2510 (2007).
 - ²⁶Strogatz, S. H. *Nonlinear Dynamics and Chaos: With Applications to Physics, Biology, Chemistry, and Engineering*, (Routledge Taylor and Francis Group, Oxford, UK 1994).
 - ²⁷Schmidt, L. & Krischer, K. Two-cluster solutions in an ensemble of generic limit-cycle oscillators with periodic self-forcing via the mean-field. *Phys. Rev. E* **90**, 042911 (2014).
 - ²⁸Sorrentino, F., Pecora, L. M., Hagerstrom, A. M., Murphy, T. E. & Roy, R. Complete characterization of the stability of cluster synchronization in complex dynamical networks. *Sci. Adv.* **2**, 1–9 (2016).
 - ²⁹Newhouse, S., Ruelle, D. & Takens, F. Occurrence of strange Axiom A attractors near quasi periodic flows on T^m , $m \geq 3$. *Commun. Math. Phys.* **64**, 35–40 (1978).
 - ³⁰Chossat, P. & Golubitsky, M. Symmetry-increasing bifurcation of chaotic attractors. *Phys. D Nonlinear Phenom.* **32**, 423–436 (1988).
 - ³¹Kaneko, K. Dominance of Milnor attractors in globally coupled dynamical systems with more than 7 ± 2 degrees of freedom. *Phys. Rev. E* **66**, 055201 (2002).
 - ³²Kaneko, K. & Tsuda, I. Chaotic itinerancy. *Chaos* **13**, 926–936 (2003).
 - ³³Schmidt, L. & Krischer, K. Chimeras in globally coupled oscillatory systems: From ensembles of oscillators to spatially continuous media. *Chaos* **25**, 64401 (2015).
 - ³⁴Miethe, I., García-Morales, V. & Krischer, K. Irregular subharmonic cluster patterns in an autonomous photoelectrochemical oscillator. *Phys. Rev. Lett.* **102**, 194101 (2009).
 - ³⁵Miethe, I. & Krischer, K. Ellipsomicroscopic studies of the anodic oxidation of p-type silicon in fluoride containing electrolytes during current oscillations. *J. Electroanal. Chem.* **666**, 1–10 (2012).
 - ³⁶Schönleber, K. & Krischer, K. High-amplitude versus low-amplitude current oscillations during the anodic oxidation of p-type silicon in fluoride containing electrolytes. *ChemPhysChem* **13**, 2989–2996 (2012).
 - ³⁷Schönleber, K., Zensen, C., Heinrich, A. & Krischer, K. Pattern formation during the oscillatory photoelectrodissolution of n-type silicon: Turbulence, clusters and chimeras. *New J. Phys.* **16**, 063024 (2014).
 - ³⁸Schönleber, K. *Self-organization phenomena during the electrodis-solution of silicon*. Dissertation, Technische Universität München (2015).
 - ³⁹Schönleber, K., Patzauer, M. & Krischer, K. A comparison of modeling frameworks for the oscillatory silicon electrodis-solution. *Electrochim. Acta* **210**, 346–351 (2016).
 - ⁴⁰Patzauer, M., Hueck, R., Tosolini, A., Schönleber, K. & Krischer, K. Autonomous Oscillations and Pattern Formation with Zero External Resistance during Silicon Electrodis-solution. *Electrochim. Acta* **246**, 315–321 (2017).
 - ⁴¹Tosolini, A., Patzauer, M. & Krischer, K. Bichaoticity induced by inherent birhythmicity during the oscillatory electrodis-solution of silicon. *Chaos* **29**, 043127 (2019).
 - ⁴²Zhang, X. G. *Electrochemistry of Silicon and Its Oxide*, (Kluwer Academic, New York 2001).
 - ⁴³Rotermund, H. H., Haas, G., Franz, R. U., Tromp, R. M. & Ertl, G. Imaging pattern formation in surface reactions from ultrahigh vacuum up to atmospheric pressures. *Science (80-.)*. **270**, 608–610 (1995).
 - ⁴⁴Kemeth, F. P., Haugland, S. W. & Krischer, K. Symmetries of Chimera States. *Phys. Rev. Lett.* **120**, 214101 (2018).
 - ⁴⁵Fiedler, B., Haugland, S. W., Kemeth, F. & Krischer, K. Global 2-cluster dynamics under large symmetric groups. *arXiv* 2008.06944 (2020).
 - ⁴⁶Oliphant, T. E. Python for scientific computing. *Comput. Sci. Eng.* **9**, 10–20 (2007).
 - ⁴⁷Virtanen, P. et al. SciPy 1.0: fundamental algorithms for scientific computing in Python. *Nat. Methods* **17**, 261–272 (2020).
 - ⁴⁸Van Der Walt, S., Colbert, S. C. & Varoquaux, G. The NumPy array: A structure for efficient numerical computation. *Comput. Sci. Eng.* **13**, 22–30 (2011).
 - ⁴⁹Hunter, J. D. Matplotlib: A 2D graphics environment. *Comput. Sci. Eng.* **9**, 90–95 (2007).
 - ⁵⁰Doedel, E. J. AUTO: A program for the automatic bifurcation analysis of autonomous systems. *Congr. Numer* **30**, 265–284 (1981).
 - ⁵¹Doedel, E. & Oldeman, B. *Auto 07p: Continuation and bi-furcation software for ordinary differential equations*. Technical report. Tech. rep., Concordia University and McGill HPC Centre, Montreal, Canada (2019).

METHODS

Stuart-Landau oscillators

The differential equations (1) were solved numerically using the Python programming language⁴⁶ (version 2.7 and later 3.8) and the implicit Adams method of the `scipy.integrate.ode` class of the SciPy library⁴⁷ (version 1.6) with a time step of $\Delta t = 0.01$. The data were held and processed in the form of NumPy (version 1.19) arrays⁴⁸ with complex-valued floating-point elements and visualized using the Matplotlib library and graphics environment (version 3.3)⁴⁹. The numerical results were

evaluated using custom-built functions drawing on the resources of these standard Python libraries, written by S.W.H. Simulations were carried out in the non-rotating frame of equation (1), and results in the co-rotating frame of $\langle W \rangle$ were visualized applying equation (3) to the data *after* simulations had been carried out. When not otherwise stated, initial conditions of numerical solutions were random numbers on the real line, fulfilling the global constraint that $\langle W \rangle = \eta e^{-i\nu t}$. This choice was inspired by earlier work¹⁷.

Figs. 1e and 2c were created using the dynamical-systems continuation software Auto07p^{50,51} to continue solutions in parameter space. As Auto can only continue fixed-point and limit-cycle solutions, equation (1) had to be formulated in the co-rotating frame of the ensemble average in order to carry out these continuations, yielding

$$\begin{aligned} \frac{da_k}{dt} &= a_k - \nu b_k - \eta^2 [A_k - c_2 B_k] \\ &\quad + \frac{1}{N} \eta^2 \sum_j [A_j - c_2 B_j], \\ \frac{db_k}{dt} &= b_k + \nu a_k - \eta^2 [B_k + c_2 A_k] \\ &\quad + \frac{1}{N} \eta^2 \sum_j [B_j + c_2 A_j], \end{aligned} \quad (6)$$

where $w_k = a_k + ib_k$ with $a_k, b_k \in \mathbb{R}$, $k = 1, \dots, N$, and

$$\begin{aligned} A_k &= 3a_k + 3a_k^2 + a_k^3 + a_k b_k^2 + b_k^2, \\ B_k &= b_k + 2a_k b_k + a_k^2 b_k + b_k^3. \end{aligned} \quad (7)$$

To obtain Fig. 2c, the relevant $N = 16$ quasiperiodic solutions were first generated using Python simulations. The output data were transferred to the rotating frame, and a time series corresponding to one full period in that frame was used as input for a c_2 or η one-parameter continuation of each periodic solution, in order to detect the location of the depicted bifurcations. Then, the detected bifurcations were two-parameter continued in c_2 and η to obtain the depicted bifurcation lines.

To obtain Fig. 1e, equation (6) was reduced to a two-cluster model by setting $a_k = a_{c1}$ and $b_k = b_{c1}$ for all $k = 1, \dots, N_1$, where $w_{c1} = a_{c1} + ib_{c1}$ is the value of the first cluster. All other oscillators $k = N_1 + 1, \dots, N$ are in the other cluster $w_{c2} = a_{c2} + ib_{c2}$. This yields the following equation for the first cluster

$$\begin{aligned} \frac{da_{c1}}{dt} &= a_{c1} - \nu b_{c1} \\ &\quad + \eta^2 \left(1 - \frac{N_1}{N}\right) [A_{c2} - A_{c1} - c_2 (B_{c2} - B_{c1})], \\ \frac{db_{c1}}{dt} &= b_{c1} + \nu a_{c1} \\ &\quad + \eta^2 \left(1 - \frac{N_1}{N}\right) [c_2 (A_{c2} - A_{c1}) + B_{c2} - B_{c1}], \end{aligned} \quad (8)$$

with A_{c1} and B_{c1} analogous to equation (7), while $w_{c2} = \frac{N_1}{N-N_1} w_{c1}$, because of the constraint that $\sum_k w_k = 0$. Thus, the reduced two-cluster model is only two-dimensional. The relative size of the first cluster, N_1/N , becomes an effective fourth parameter, in addition to c_2 , ν and η .

Whereas (8) describes the motion of two clusters of sizes N_1 and $N_2 = N - N_1$, respectively, it says nothing about intra-cluster stability and cannot model the breakup of either cluster. To be able to evaluate the internal stability of the clusters, we followed Ku et al.²² and added two effectively infinitesimal extra oscillators to the model, which only feel the presence of the two macroscopic clusters, but themselves neither affect the movement of each other, nor that of the macroscopic clusters. Their motion is given by

$$\begin{aligned} \frac{dp_{1,2}}{dt} &= p_{1,2} - \nu q_{1,2} - \eta^2 [P_{1,2} - c_2 Q_{1,2}] \\ &\quad + \eta^2 \left[\frac{N_1}{N} (A_{c1} - c_2 B_{c1}) \right. \\ &\quad \left. + \frac{N - N_1}{N} (A_{c2} - c_2 B_{c2}) \right], \\ \frac{dq_{1,2}}{dt} &= q_{1,2} + \nu p_{1,2} - \eta^2 [Q_{1,2} + c_2 P_{1,2}] \\ &\quad + \eta^2 \left[\frac{N_1}{N} (B_{c1} + c_2 A_{c1}) \right. \\ &\quad \left. + \frac{N - N_1}{N} (B_{c2} + c_2 A_{c2}) \right], \end{aligned} \quad (9)$$

where $P_{1,2}$ and $Q_{1,2}$ denote composite expressions for the first and second infinitesimal oscillator, of the same form as $A_{c1,c2}$ and $B_{c1,c2}$:

$$\begin{aligned} P_{1,2} &:= 3p_{1,2} + 3(p_{1,2})^2 + (p_{1,2})^3 \\ &\quad + p_{1,2}(q_{1,2})^2 + (q_{1,2})^2, \\ Q_{1,2} &:= q_{1,2} + 2p_{1,2}q_{1,2} + (p_{1,2})^2 q_{1,2} + (q_{1,2})^3. \end{aligned} \quad (10)$$

In the initial state of the continuation, one of these two infinitesimal oscillators is set to follow the same periodic orbit as either of the two clusters. If any bifurcations are detected to make either infinitesimal oscillator leave the macroscopic cluster it started at, this means that cluster has become unstable.

Fig. 3a was created by initializing the $N = 16$ ensemble in the 8-4-4 configuration at $c_2 = -0.715$ and incrementing c_2 by $\Delta c_2 = 10^{-5}$ every $\Delta T = 4 \cdot 10^4$ time steps until $c_2 = -0.7095$ for $\nu = 0.1$ and $\eta = 0.63$. At the beginning of each c_2 step, random numbers $\leq 10^{-6}$ were added to the real and imaginary part of each oscillator to provoke the breakup of potential unstable clusters. Maxima of $\text{Re}(w_k)$ were plotted for the last 2000 time steps of simulation at each c_2 steps.

The schematic in Fig. 3b was drawn based on automatically detected cluster sizes at each c_2 step in

the aforementioned c_2 -incremented simulation. These cluster sizes were determined by calculating the pairwise cross-correlations of the trajectories of all oscillators over the last 2000 time steps at each c_2 step, respectively. If the cross-correlation differed from 1 by less than $\epsilon = 10^{-8}$, the two oscillators were deemed to belong to the same cluster. To calculate the cross-correlations and obtain the clusters, we used SciPy's built-in `scipy.cluster.hierarchy.linkage` function.

The schematic in Fig. 3c was determined based on an analogous c_2 -incremented simulations for $N = 32$, $\nu = 0.1$ and $\eta = 0.63$, initialized in the 16–16 configuration at $c_2 = -0.74$. Here, $\Delta c_2 = 2 \cdot 10^{-5}$ and $\Delta T = 10^4$. The simulation was performed until $c_2 = -0.712$, producing the result in Supplementary Figure 1a. Clusters were calculated as in the $N = 16$ case based on the last 800 time steps of simulation at each c_2 step, producing Supplementary Figure 2b.

The schematic in Fig. 3d was determined based on two analogous c_2 -incremented simulations for $N = 256$, $\nu = 0.1$ and $\eta = 0.63$. In the first of these, the ensemble was initialized in the 128–64–64 configuration at $c_2 = -0.7145$, from where c_2 was incremented by $\Delta c_2 = 10^{-5}$ every $\Delta T = 2 \cdot 10^4$ time steps until $c_2 = -0.7117$, producing the result in Supplementary Figure 2a. In a second c_2 -incremented simulation for $N = 256$, the ensemble was initialized at $c_2 = -0.71172$ in the 128–64–33–16–15 configuration found there in the prior $N = 256$ simulation with $\Delta c_2 = 10^{-5}$. From there on, c_2 was incremented by $\Delta c_2 = 2 \cdot 10^{-7}$ every $\Delta T = 2 \cdot 10^4$ time steps until $c_2 = -0.7116$, producing the result in Supplementary Figure 3a-b. For either simulation, clusters were calculated based on the last 800 time steps of simulation at each c_2 step, producing Supplementary Figures 2b and 3b-c, respectively.

Fig. 5b-d were created by simulating the 16–9–(7×1) solution in Fig. 5a for $T = 10^6$ time steps. Every 10^4 time steps, the pairwise cross-correlation between all oscillators was calculated over an interval of 800 time steps, and if the cross-correlation of two oscillators was found to be greater than $1 - \epsilon$ for $\epsilon = 10^{-8}$ (Fig. 5b), $\epsilon = 10^{-4}$ (Fig. 5c) or $\epsilon = 10^{-2}$ (Fig. 5d), respectively, they were counted as being in the same cluster.

The solutions in Fig. 6 were obtained by initializing the $N = 20$ ensemble in a 15–5 solution at $c_2 = -0.88$, $\nu = 0.1$ and $\eta = 0.67$, and incrementing c_2 by $\Delta c_2 = 2 \cdot 10^{-4}$ every $\Delta T = 5000$ time steps until $c_2 = -0.7$. Supplementary Figures 4 to 7 were created based on data obtained analogously to that in Figs. 3 and 6 with parameters as given in their respective captions.

Pitchfork maps

The differential equations (1) were solved numerically using the Python programming language⁴⁶ (version 3.8). The data were held and processed in the form of NumPy (version 1.19) arrays⁴⁸ with complex-valued floating-point

elements and visualized using the Matplotlib library and graphics environment (version 3.3)⁴⁹. The numerical results were evaluated using custom-built functions drawing on the resources of these standard Python libraries, written by S.W.H.

The α -incremented simulations behind Fig. 8 were initialized in the $N/2 - N/2$ configuration and α was then gradually increased as specified in the captions of Supplementary Figs. 9 and 10. The same applies to Supplementary Fig. 11. At the beginning of each α step, small random numbers $\leq 10^{-6}$ were added to the maps to provoke the breakup of potential unstable clusters.

The cluster sizes at each α step of the aforementioned simulations were calculated automatically by comparing the trajectories of all maps during the last 2000 steps at each α value. If the Euclidean distance between the vectors made up by two such map trajectories was found to be less than $\epsilon = 10^{-4}$, the two maps were said to be in the same cluster.

Electrochemical experiments

For the experiments a custom made three electrode electrochemical PTFE cell is used, with a circular shaped platinum wire as counter electrode and a commercial mercury-mercurous sulfate reference electrode³⁴. As working electrode a sample from a n-type Silicon wafer with a (111) crystal orientation and a resistivity of 1-10 Ωcm is used. It is prepared and mounted to the electrode holder according to^{34,36}. The organic cleaning solvents are AnalaR NORMAPUR grade (VWR Chemicals). The electrolyte components are Suprapur grade (Merck). For the potential control a FHI-2740 potentiostat is used. Illumination of the electrode is provided by a 15 mW HeNe laser with a wavelength of 632.8 nm (Thorlabs HNL150L). The illumination intensity is controlled by an SLM (Hamamatsu x10468-06). The ellipsometric signal is recorded with a JAI-CV-A50 CCD camera.

The experimental data presented is obtained from experiments under the following conditions: The electrolyte used for Fig.9 a) and b) had a pH of 2.3 and a fluoride concentration $c_F = 50 \text{ mM}$. For a) the applied potential was $U = 5.65 \text{ V vs SHE}$, the external resistance times electrode area $R_{\text{ext}}A_{\text{el}} = 0 \text{ k}\Omega\text{cm}^2$ and the illumination intensity $I_{\text{ill}} = 0.67 \text{ mW/cm}^2$. For b) $U = 6.65 \text{ V vs SHE}$, $R_{\text{ext}}A_{\text{el}} = 3.84 \text{ k}\Omega\text{cm}^2$, $I_{\text{ill}} = 0.57 \text{ mW/cm}^2$. The electrolyte used for c) and d) had a pH of 1 and a fluoride concentration of $c_F = 75 \text{ mM}$. For c) the applied potential was $U = 8.65 \text{ V vs SHE}$, the external resistance times electrode area $R_{\text{ext}}A_{\text{el}} = 0.81 \text{ k}\Omega\text{cm}^2$ and the illumination intensity $I_{\text{ill}} = \text{mW/cm}^2$. For d) $U = 8.65 \text{ V vs SHE}$, $R_{\text{ext}}A_{\text{el}} = 0.54 \text{ k}\Omega\text{cm}^2$, $I_{\text{ill}} = 0.57 \text{ mW/cm}^2$. The illumination on the working electrode was homogeneous at any time.

ACKNOWLEDGMENTS

The authors thank Felix P. Kemeth, Maximilian Patzauer and Seungjae Lee for fruitful discussions. Financial support from the Studienstiftung des deutschen Volkes and the Deutsche Forschungsgemeinschaft, project KR1189/18 “Chimera States and Beyond”, is gratefully acknowledged.

AUTHOR CONTRIBUTIONS

S.W.H. carried out the simulations and analysed the numerical data. A.T. performed the experiments and

analysed the experimental data. All three authors discussed the results and wrote the paper. K.K. supervised the project.

COMPETING INTERESTS

The authors declare no competing interests.

Supplementary Information: Between Synchrony and Turbulence: Intricate Hierarchies of Coexistence Patterns

Sindre W. Haugland, Anton Tosolini, and Katharina Krischer^{a)}

Physics Department, Nonequilibrium Chemical Physics, Technical University of Munich, James-Frank-Str. 1, D-85748 Garching, Germany

(Dated: 30 December 2021)

The following Supplementary Figures as well as the sections describing the reasoning behind them are presented in the order the main manuscript addresses these figures.

c_2 -INCREMENTED SIMULATIONS BEHIND THE SCHEMATICS IN FIG. 3 B-D

Like the schematic in Fig. 3b is based on the quantitative simulation in Fig. 3a, the schematic in Fig. 3c is based on the quantitative simulation in Supplementary Fig. 1, and the schematic in Fig. 3d is based on the quantitative simulations in Supplementary Figs. 2 and 3.

In Supplementary Fig. 1, the $N = 32$ ensemble is initialized in a 16–16 configuration at $c_2 = -0.74$, $\nu = 0.1$ and $\eta = 0.63$. This corresponds to the very left of the figure, from where c_2 was incremented by $\Delta c_2 = 2 \cdot 10^{-5}$ every $\Delta T = 10^4$ time steps. The upper part of the figure depicts how the maxima of the real part of each oscillator evolve in the co-rotating frame of the ensemble average $\langle W \rangle = \eta e^{-i\nu t}$. The lower part depicts the sizes of clusters automatically detected at each c_2 step. Further details are given in the figure caption.

In Supplementary Fig. 2, the $N = 256$ ensemble is initialized in a 128–64–64 configuration at $c_2 = -0.7145$, $\nu = 0.1$ and $\eta = 0.63$. This corresponds to the very left of the figure, from where c_2 was incremented by $\Delta c_2 = 10^{-5}$ every $\Delta T = 2 \cdot 10^4$ time steps. Again, the upper part of the figure depicts how the maxima of the real part of each oscillator evolve in the co-rotating frame of the ensemble average $\langle W \rangle = \eta e^{-i\nu t}$. The lower part depicts the sizes of clusters automatically detected at each c_2 step. Further details are given in the figure caption.

Supplementary Fig. 3 depicts a continuation of the c_2 -incremented simulation in Supplementary Fig. 2 with the far smaller c_2 step $\Delta c_2 = 2 \cdot 10^{-7}$. In the very left part of this figure, at $c_2 = -0.71172$, the ensemble was initialized in the 128–64–33–16–15 state found there in the prior c_2 -incremented simulation depicted in Supplementary Fig. 2. Further details are given in the figure caption.

REVERSE $N = 16$ SIMULATION

Fig. 3a-b of the main article shows the transition from 8–4–4 period-2 motion in the rotating frame via 8–4–2–2 period-4 motion, 8–4–(4×1) period-8 motion and 8–4–(4×1) quasiperiodic motion to 8–4–(4×1) itinerant motion. On this route, the ensemble passes through two period-doubling, a torus and a symmetry-increasing bifurcation. Supplementary Fig. 4 shows that the sequence and occurrence of bifurcations is the same if we initialize the ensemble in the 8–4–(4×1) itinerant solution and move the opposite way through parameter space. There is no hysteresis here.

Only if a parameter-incremented simulation is carried out so far that the ensemble eventually jumps to a different branch will we observe hysteresis. For example, if the $N = 32$ ensemble were initialized in one of the states for $c_2 > -0.628$ in Fig. 5 and c_2 were gradually decreased from there, the ensemble would not move back along the 16–9–7-derived branch. Rather, it would either stay on the 16–8–8-derived branch (if initialized at $-0.628 < c_2 < -0.627$) or on the 27–2–1–1–1-branch depicted in Fig. 6 (if initialized in the incoherent region $c_2 > -0.627$).

SYMMETRY-BREAKING BIFURCATIONS TO FULL INCOHERENCE

For $\nu = 0.1$ and $\eta = 0.63$, c_2 -incremented simulations like those in Fig. 3a and Supplementary Fig. 1 do not create stable states of fully incoherent single oscillators at the end of the depicted bifurcation cascades. Instead, the ensemble will at some point jump to some other cluster-solution that is co-stable with the last step of the simulated cascade. If for example the $N = 16$ c_2 -incremented simulation in Fig. 3a is continued further, the ensemble at some point is thrown onto a 5–3–5–3 four-cluster solution. This 5–3–5–3 is actually even co-stable with all steps of the cascade from the 8–4–4 state onward, as can be deduced from the dashed line in Fig. 2c, where the 5–3–5–3 solution is stable below the dashed green pitchfork bifurcation line of the 8–5–3 state. Analogously, the $N = 32$ c_2 -incremented simulation in Supplementary Fig. 1, jumps to a 10–6–10–6 solution shortly to the right of the depicted c_2 interval.

For $\eta = 0.67$, the situation is different, as no $N/2$ – $N/2$ -derived four-cluster solutions like the 10–6–10–6 solution are stable beyond the end of an equivalent cluster-

^{a)}Electronic mail: krischer@tum.de

splitting cascade. This is illustrated in Supplementary Fig. 5, where the ensemble, when c_2 -incremented from the 16–16 state at $c_2 = -0.6425$, first assumes a 16–9–7 solution and then goes through a sequence of bifurcations similar to that in Supplementary Fig. 1. As indicated by the cluster sizes in the lower part of the figure, it at some point ends up in a 16–9–(7×1) configuration. From there on, it jumps to a 16–8–4–4 solution. This solution is part of a the different somewhat longer-lasting cascade via the 16–8–8 solution that is co-stable with the cascade via the 16–9–7 solution that the ensemble originally went through here. Even further upward in c_2 , no $N/2$ – $N/2$ -derived solutions are stable anymore, and the dynamics consequently become fully incoherent. (Whereas it might appear from the lower part of the figure as if there still exist various non-trivial clusters $N_i > 1$ for $c_2 \approx -0.626$, in particular of sizes $N_1 = 2, 3$, these are actually only precision-dependent approaches to ruins of former clusters, similar to those we observe in Fig. 4 of the main article.)

Before looking closer at those incoherent dynamics, we trace an entirely different path that also lead to them. This path starts at a 27–2–1–1–1 solution for which the maxima of $\text{Re}(w_k)$ are shown in the leftmost part of Supplementary Fig. 6a. The trajectories of the clusters and single oscillators of this solution in the rotating frame of $\langle W \rangle$ are shown in Supplementary Fig. 7a-b. At $c_2 \approx -0.6402$, an equivariant torus bifurcation introduces a tertiary frequency to the dynamics and explodes the cluster of 27 into a ring of single oscillators. This is reflected in the broadening of the maxima in Supplementary Fig. 6a into continuous bands. The new solution is depicted in Supplementary Fig. 7c-d.

After a sufficient further increase in c_2 the different variants of the emergent 2–(30×1) solution collide in a symmetry-increasing bifurcation, leaving only single oscillators. (While again, Supplementary Fig. 6b appears to detect several clusters $N_i > 1$, these, like in Supplementary Fig. 5b, are also just cluster ruins.) Initially, however, the resultant fully incoherent attractor is still co-stable with the cascades the ensemble goes through in Supplementary Fig. 5, as evident from the fact that the extent of the c_2 axis in the two figures is the same. This only changes shortly before we reach $c_2 = -0.626$. At this value, the incoherent dynamics incorporate attractor ruins of both the formerly stable 2–(30×1) in Supplementary Fig. 7c-d and the 16–16-derived solutions in Supplementary Fig. 5. In Supplementary Fig. 7e, the former is mirrored by the large almost circular excursions of single oscillators away from the origin. The latter is mirrored by the two more oval blue-green loops similar to those in the solutions in Fig. 2 of the main article.

PATH FROM 150–50 SOLUTION TO CHIMERA STATE

In Fig. 5 of the main article, the bifurcations from a 15–5 two-cluster solution to a 15–(5×1) chimera state

are traced exactly. For $N = 200$, initializing a 150–50 two-cluster solution at the same parameter values as in the $N = 20$ case and gradually increasing c_2 provokes a cluster-breaking cascade as well. This can be seen in Supplementary Fig. 8, which depicts two such c_2 -incremented simulations with different Δc_2 .

In the more coarsely incremented simulation in the upper half of the figure, the cluster of 50 clearly splits into a cluster of 26 and a cluster of 24. The more finely incremented simulation in the lower half is initialized in the resultant 150–26–24 configuration. A subsequent break-up of the cluster of 24 into a cluster of 13 and a cluster of 11 occurs in both simulations. In the lower half of the figure, we can also distinguish a break-up of the cluster of 11 into a cluster of 6 and a cluster of 5, as well as the later collapse of the cluster of five.

Further increases in c_2 causes the ensemble to jump between various parallel multi-cluster solution branches that all have in common that the large cluster of 150 oscillators remains intact. Eventually, the last of these multi-cluster solutions undergoes a symmetry-increasing bifurcation, creating a 150–(50×1) chimera state.

For even greater values of c_2 , the large cluster absorbs some of the single oscillators, increasing the imbalance between synchronized and single oscillators. Ultimately, the large cluster also collapses, leading to a state of full incoherence.

α -INCREMENTED SIMULATIONS BEHIND THE SCHEMATICS IN FIG. 7

In order to chart the cluster-splitting cascades and general sequences of bifurcations in the ensemble of globally coupled pitchfork maps, we performed various α -incremented simulations for fixed values of β and different ensemble sizes N . The outcome of one such α -incremented simulation for $N = 16$ is shown in Supplementary Fig. 9, where the upper part of the figure shows the range of values reached by any of the maps for each value of α . This diagram clearly shows two subsequent period-doublings of the maps inhabiting positive values $y_k(n) > 0$, followed by a Neimark-Sacker, a symmetry-increasing bifurcation and a final subcritical transition to a different solution. The lower part of the figure shows that the two period-doublings are accompanied by cluster splittings, first from an 8–8 to an 8–4–4 and then to an 8–(4×2) configuration. The symmetry-increasing bifurcation is accompanied by the appearance of single, unclustered maps.

Supplementary Fig. 10a-b shows an analogous depiction of a similar α -incremented simulation for $N = 128$, initialized in the 64–33–31 configuration. The simulation begins with three clearly discernable cluster-splitting period-doubling bifurcations, reaching a 64–33–16–8–4–3 configuration somewhat above $\alpha = 0.87$. These bifurcations are followed by a string of less easily identifiable

transitions between different solutions. Above $\alpha \approx 0.877$, persistent clusters clearly coexist with loose and temporary agglomerations, a sign of itinerant dynamics for large N , as also seen in the Stuart-Landau ensemble. Around $\alpha \approx 0.883$, the cluster of 64 is for a certain α interval the only persistent cluster, signifying a $64-(64 \times 1)$ chimera state. In Supplementary Fig. 10c, the cluster solution found at $\alpha \approx 0.87$ in Supplementary Fig. 10a-b is incremented in smaller steps of α . This shows that the initial cluster-halving cascade indeed also reaches a $64-33-16-8-4-2-1$ configuration before the larger clusters are broken.

PREMATURELY ENDING PITCHFORK-MAP CLUSTER-SPLITTING CASCADE FOR $N=256$

In the case of $N = 256$, the period-doubling cluster-splitting bifurcation of the $N/2-N/2 = 128-128$ solution also produces a $128-65-63$ solution. If this solution is traced upward in α , the cluster of 63 is split into smaller clusters of 32 and 31, analogous to the development of most of the cluster-splitting cascades described above. However, the next bifurcation encountered is not another period-doubling, but an equivariant pitchfork splitting the cluster of 65. Supplementary Fig. 11a clearly shows that thereby, the hitherto period-2 trajectories of the maps in the cluster of 65 (depicted in green) are replaced by period-4 trajectories. The result, a $128-34-31-32-31$ period-4 solution, reminds us of the $8-(4 \times 2)$ period-4 solution produced in the second period-doubling of the

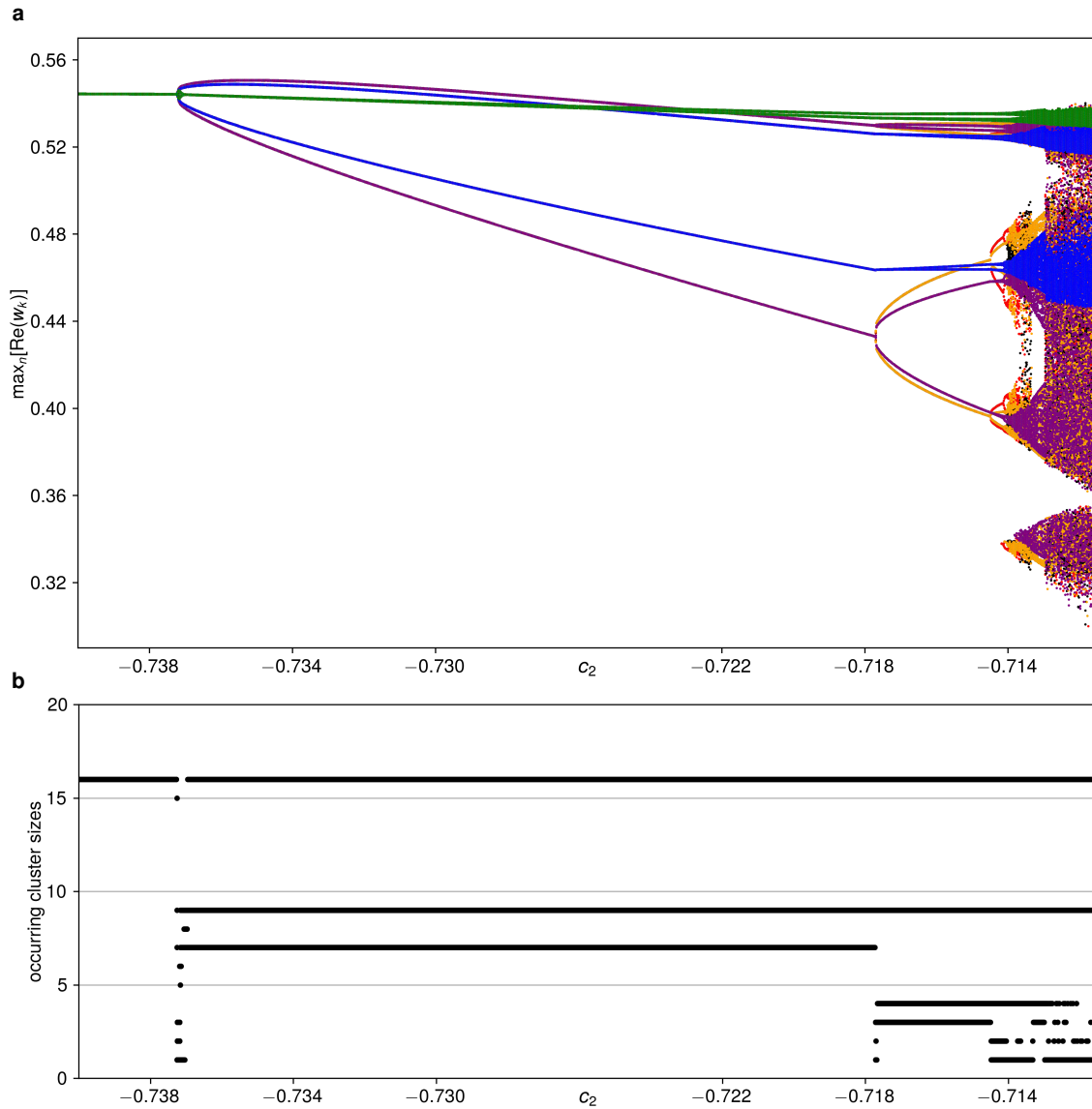
$N = 16$ ensemble in Supplementary Fig. 9. Like in that simulation, the next bifurcation in the $N = 256$ ensemble is a Neimark-Sacker bifurcation, followed by a symmetry-increasing bifurcation, as evident from the coexistence of persistent and temporary clusters from somewhat above $\alpha = 0.88$. Another symmetry-increasing bifurcation creates a $128-(128 \times 1)$ balanced chimera state.

SPATIALLY AVERAGED ELLIPSOMETRIC SIGNALS

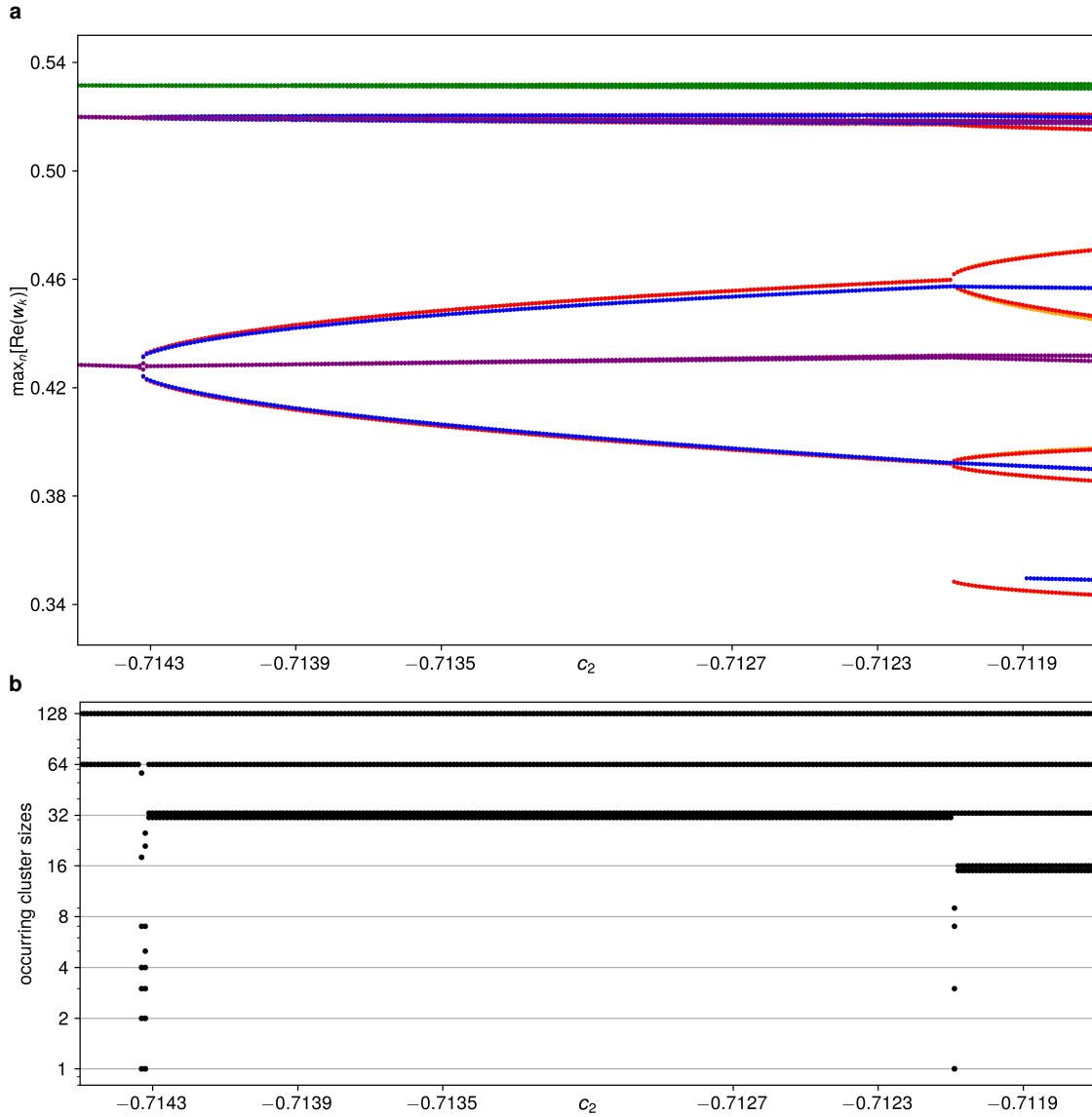
Supplementary Fig. 12 shows the timeseries of the spatial average of the ellipsometric signal normalised to its maximum ξ_{av}/ξ_{av}^{max} . The order of the states is the same as in Fig. 9 of the main manuscript, i.e., Supplementary Fig. 12a depicts the spatially averaged ellipsometric signal for the antiphase state, b for the subharmonic clustering, c for the chimera and d for the turbulent state. In each case, the periodic oscillation of the average signal is conserved, similar to the conservation law for the average value of the globally coupled Stuart-Landau oscillators. This justifies subtracting the homogeneous mode to enter a rotating frame of reference.

c_2 -INCREMENTED SIMULATION FOR ODD $N = 63$

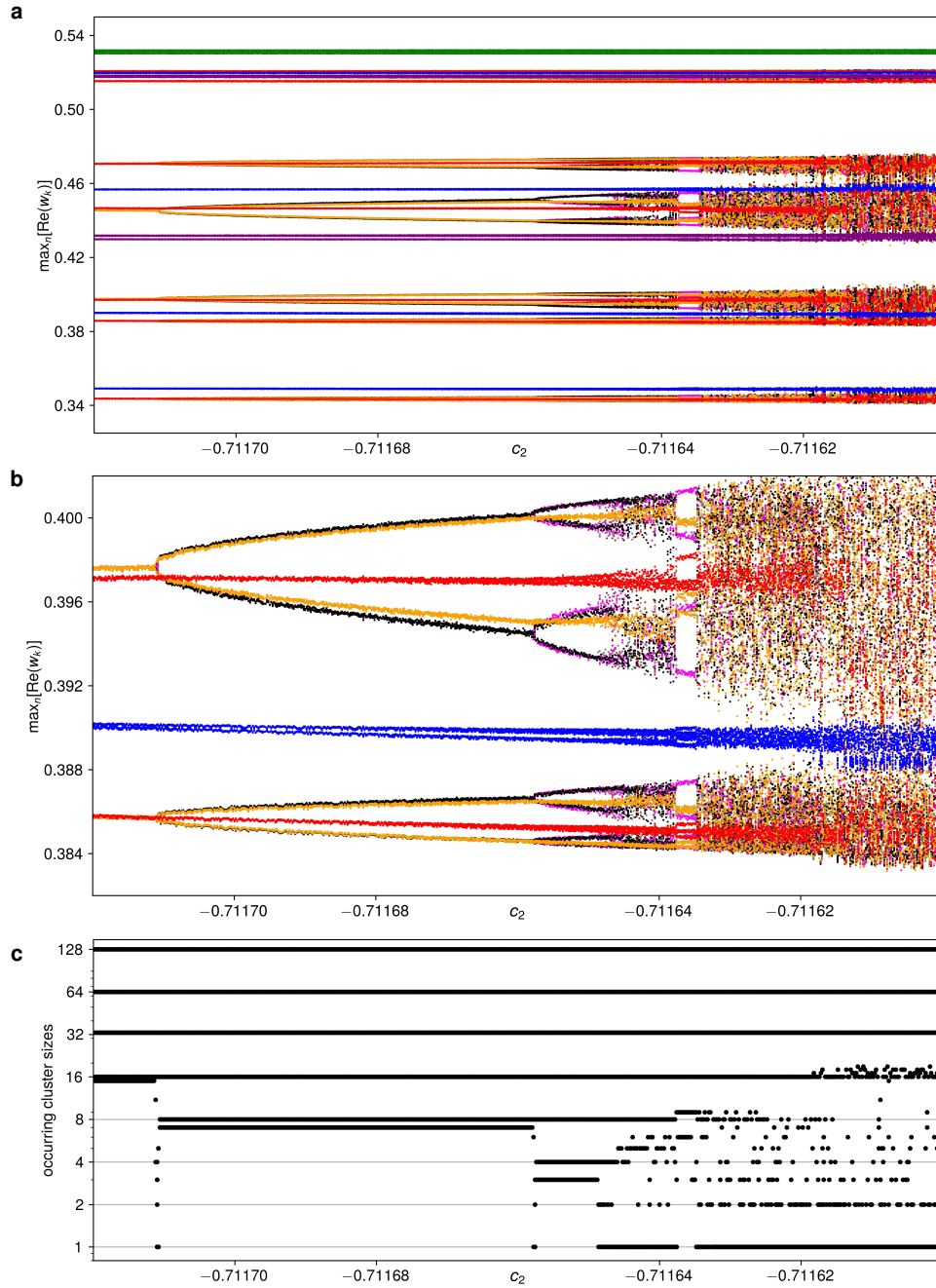
Whereas this article focuses on even ensemble sizes, its findings seem to be valid for odd N as well. In particular, Supplementary Fig. 13 shows that both the cluster-halving cascade and a subsequent symmetry-increasing bifurcation can be observed for $N = 63$.



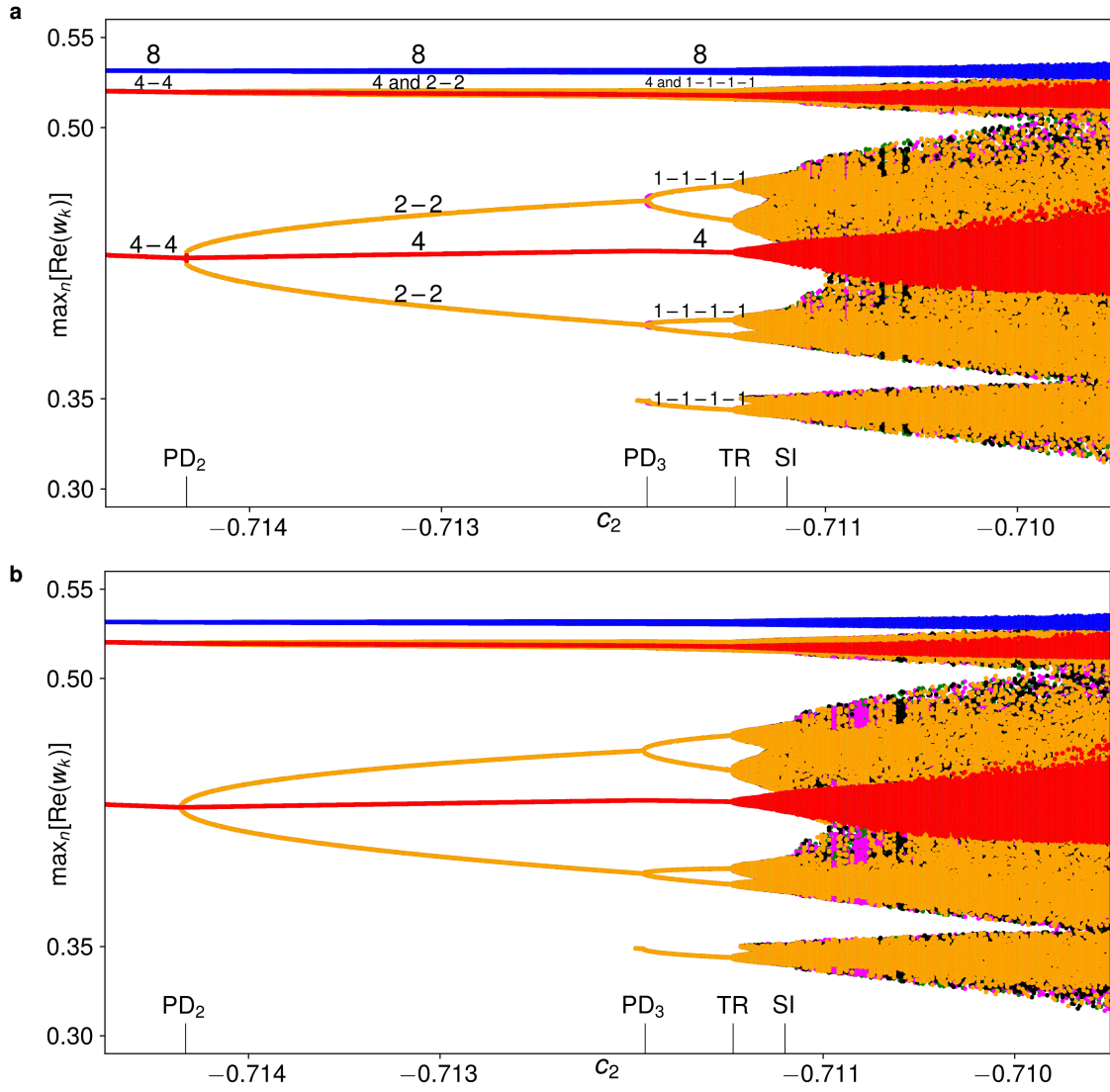
Supplementary Fig. 1. Cluster-splitting cascade and ensuing bifurcations for $N = 32$. **a**, All occurring maxima of the rotating-frame real parts $\text{Re}(w_k)$ of all clusters and single oscillators against c_2 as c_2 is gradually increased at a rate of $\Delta c_2 = 2 \cdot 10^{-5}$ every 10^4 time steps for $N = 32$, $\nu = 0.1$ and $\eta = 0.63$. Oscillators are colored by the clusters to which they belong in the cluster-splitting cascade. Initially, there are two clusters of 16, reaching a single maximum shown in green. At $c_2 \approx -0.737$, one of these clusters splits up into a cluster of nine, shown in blue, and a cluster of seven, shown in purple, that both are period-2. At $c_2 \approx -0.7177$, the cluster of seven splits up into a cluster of four (purple) and a cluster of three (yellow). At $c_2 \approx -0.7145$, the cluster of three splits up into a cluster of two (yellow) and a single oscillator (red). When the cluster of two is destroyed, the two resulting single oscillators are shown in red and black. At higher c_2 values, additional single oscillators retain the color of the cluster to which they belonged in the 16–9–4–1–1–1 solution. **b**, Cluster sizes at each value of c_2 during the c_2 -incremented simulation in **a**. Calculations are based on the cross correlations of trajectories (in the non-rotating frame) over the last 800 time steps of simulation at each c_2 value and a threshold of $\varepsilon = 10^{-8}$. See Methods section.



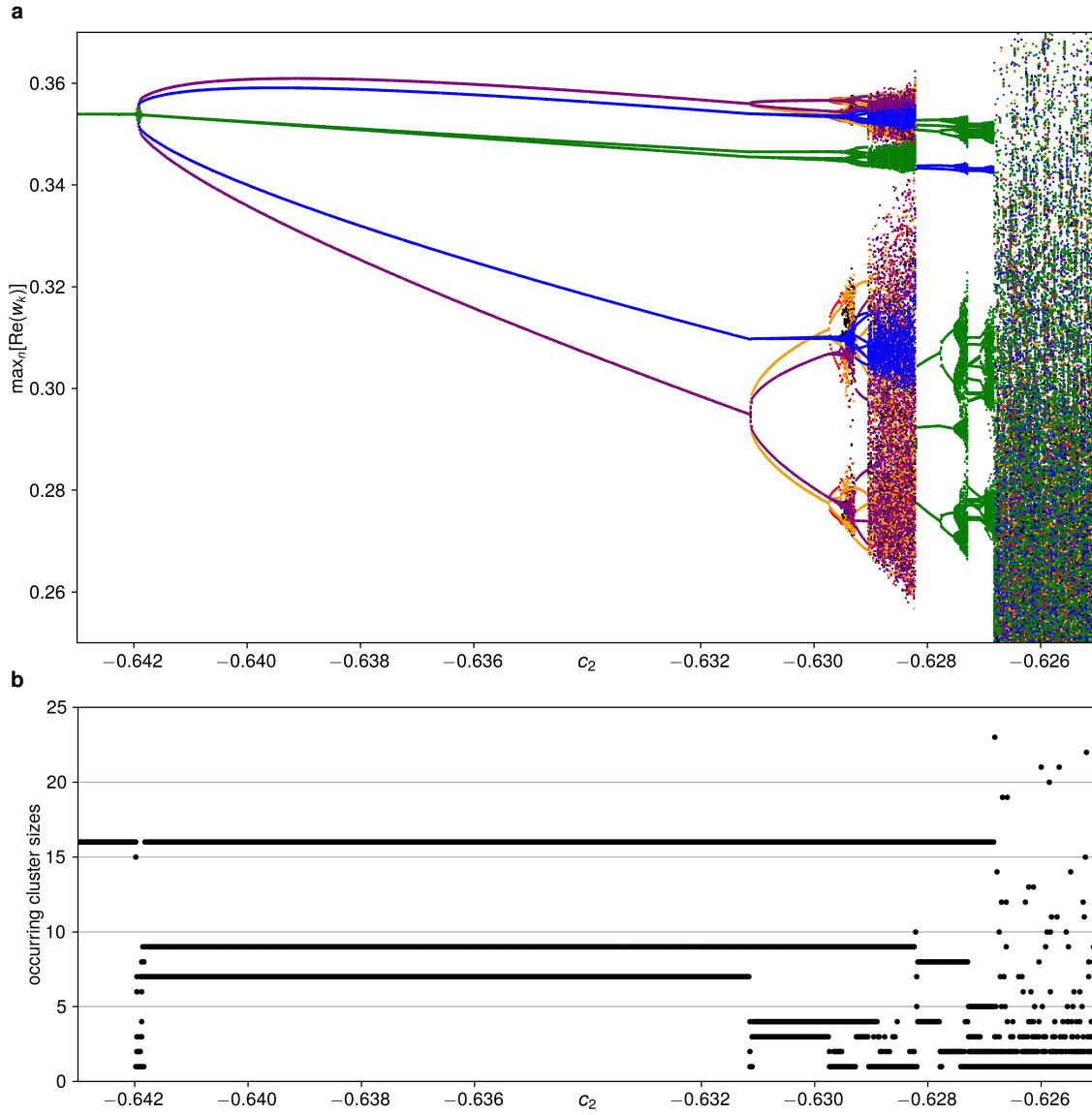
Supplementary Fig. 2. First cluster-splitting bifurcations for $N = 256$. **a**, All occurring maxima of the real parts of all clusters and single oscillators against c_2 as c_2 is gradually increased at a rate of $\Delta c_2 = 10^{-5}$ every $2 \cdot 10^4$ time steps for $N = 256$, $\nu = 0.1$ and $\eta = 0.63$. The simulation is initialized in the 128–64–64 solution at $c_2 = -0.7145$. Oscillators are colored by the clusters to which they belong in the final 128–64–33–16–15 solution: In the leftmost part of the figure, the maxima of the cluster of 128 are shown in green, the maxima of the two clusters of 64 in purple. At $c_2 \approx -0.7143$, one of these clusters splits up into a cluster of 33 (blue) and a cluster of 31 (red). At $c_2 \approx -0.7121$, the cluster of 31 splits up into a cluster of 16 (red) and a cluster of 15 (yellow). **b**, Cluster sizes at each value of c_2 during the c_2 -incremented simulation in **a**. Calculations are based on the cross correlations of trajectories (in the non-rotating frame) over the last 800 time steps of simulation at each c_2 value and a threshold of $\varepsilon = 10^{-8}$. See Methods section. The vertical axis scales logarithmically.



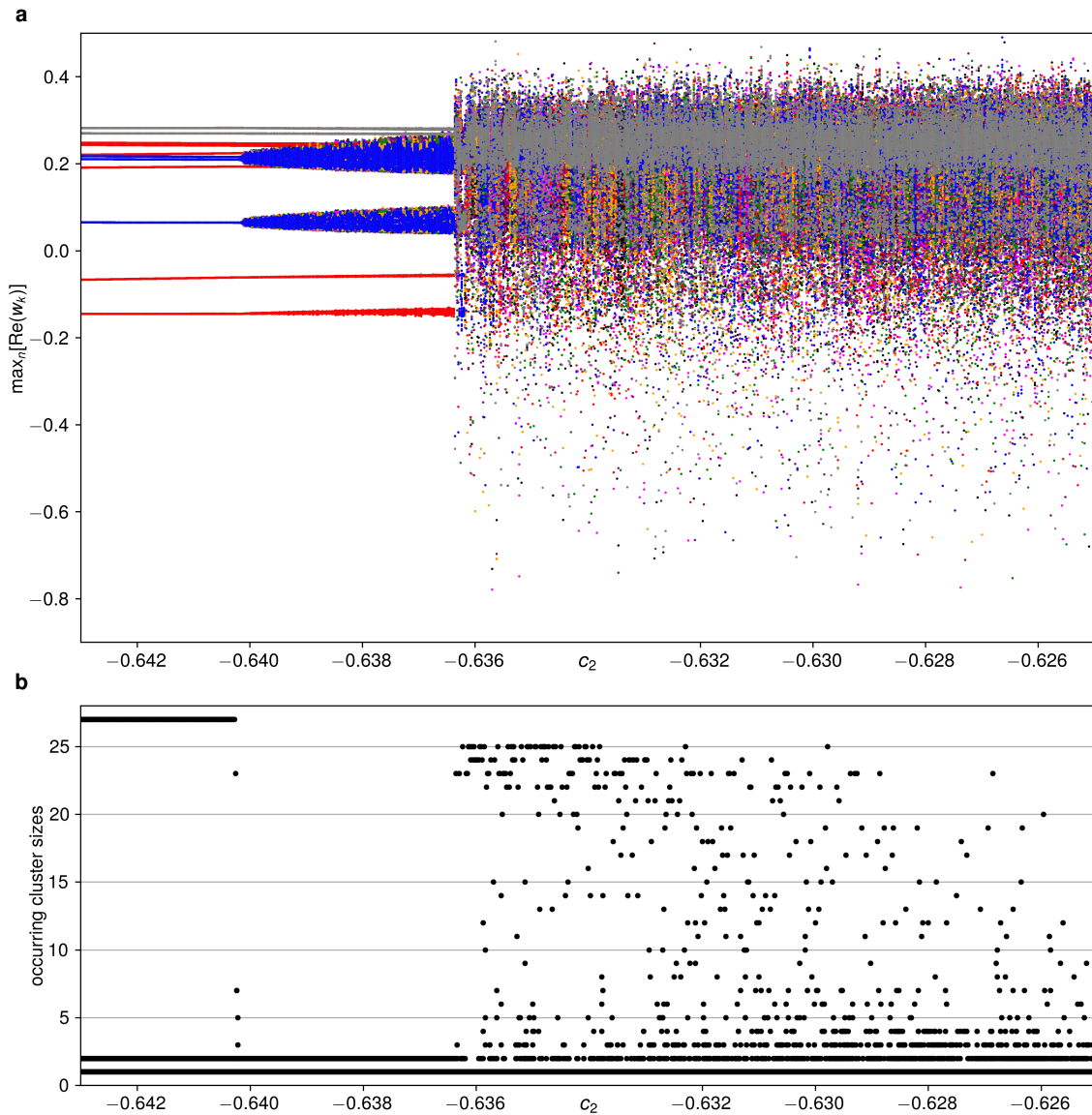
Supplementary Fig. 3. Continued cluster-splitting cascade and ensuing bifurcations for $N = 256$. **a**, All occurring maxima of the real parts of all clusters and single oscillators against c_2 as c_2 is gradually increased at a rate of $\Delta c_2 = 2 \cdot 10^{-7}$ every $2 \cdot 10^4$ time steps for $N = 256$, $\nu = 0.1$ and $\eta = 0.63$. The simulation is initialized in the 128–64–33–16–15 solution found at $c_2 = -0.71172$ in Supplementary Fig. 2. In the leftmost part of the figure, the maxima of the clusters of 128, 64, 33, 16 and 15 are shown in green, purple, blue, red and yellow, respectively. At $c_2 \approx -0.71171$, the cluster of 15 splits up into a cluster of eight (yellow) and a cluster of seven (black). At $c_2 \approx -0.71166$, the cluster of seven splits up into clusters of four and three (in black and pink, respectively). At $c_2 \approx -0.71165$, the cluster of three splits up into a cluster of two (pink) and a single oscillator (grey), manifest only in the appearance of additional grey dots and easier seen in **c**. At higher c_2 values, additional single oscillators retain the color of the cluster to which they belonged in the 128–64–33–16–8–4–2–1 solution. **b**, Magnified view of the maxima $0.382 < \max_n[\text{Re}(w_k)] < 0.404$ in **a**. **c**, Cluster sizes at each value of c_2 during the simulation in **a**, **b**. Calculations are based on the last 800 time steps of simulation at each c_2 value and a threshold of $\varepsilon = 10^{-8}$. See Methods section. The vertical axis scales logarithmically.



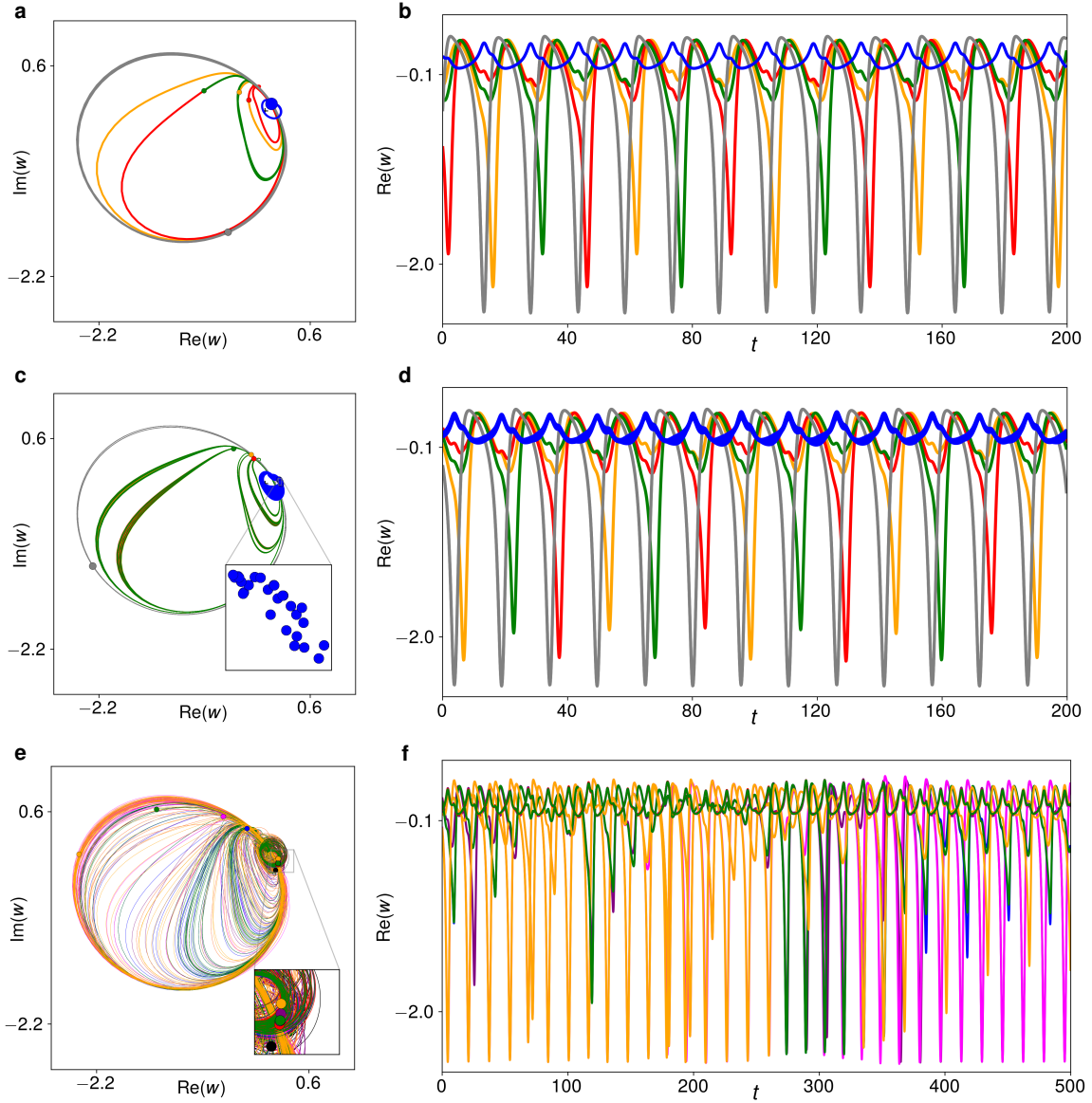
Supplementary Fig. 4. c_2 -incremented and decremented simulations for $N = 16$. **a**, Maxima of $\text{Re}(w_k)$ against c_2 as c_2 is gradually increased at a rate of $\Delta c_2 = 10^{-5}$ every $4 \cdot 10^4$ time steps for $\eta = 0.63$. This figure is also included in the main manuscript as Fig. 3 a. Labels on the figure mark the clusters reaching the different maxima as the solution changes from 8–4–4 via 8–4–2–2 to 8–4–(4×1). Labels on the abscissa mark occurring period-doubling (PD), torus (TR) and symmetry-increasing (SI) bifurcations. The additional smallest yellow maximum appearing at $c_2 \approx -0.712$ is caused by the continuous deformation of the oscillator trajectories and not by a bifurcation. At $c_2 \approx -0.7115$, the torus bifurcation to three-frequency dynamics manifests itself in a distinct broadening of the formerly discrete maxima. **b**, Maxima of $\text{Re}(w_k)$ as c_2 is gradually *decreased* at a rate of $\Delta c_2 = -10^{-5}$ every $4 \cdot 10^4$ time steps after initializing the ensemble at the right edge of **a**. In the itinerant parameter region $c_2 > -0.7112$, recorded maxima and transient clusters differ for the two solutions, but the qualitative dynamics are the same. Moreover, all indicated bifurcations (PD, TR and SI) occur at the respective same parameter values.



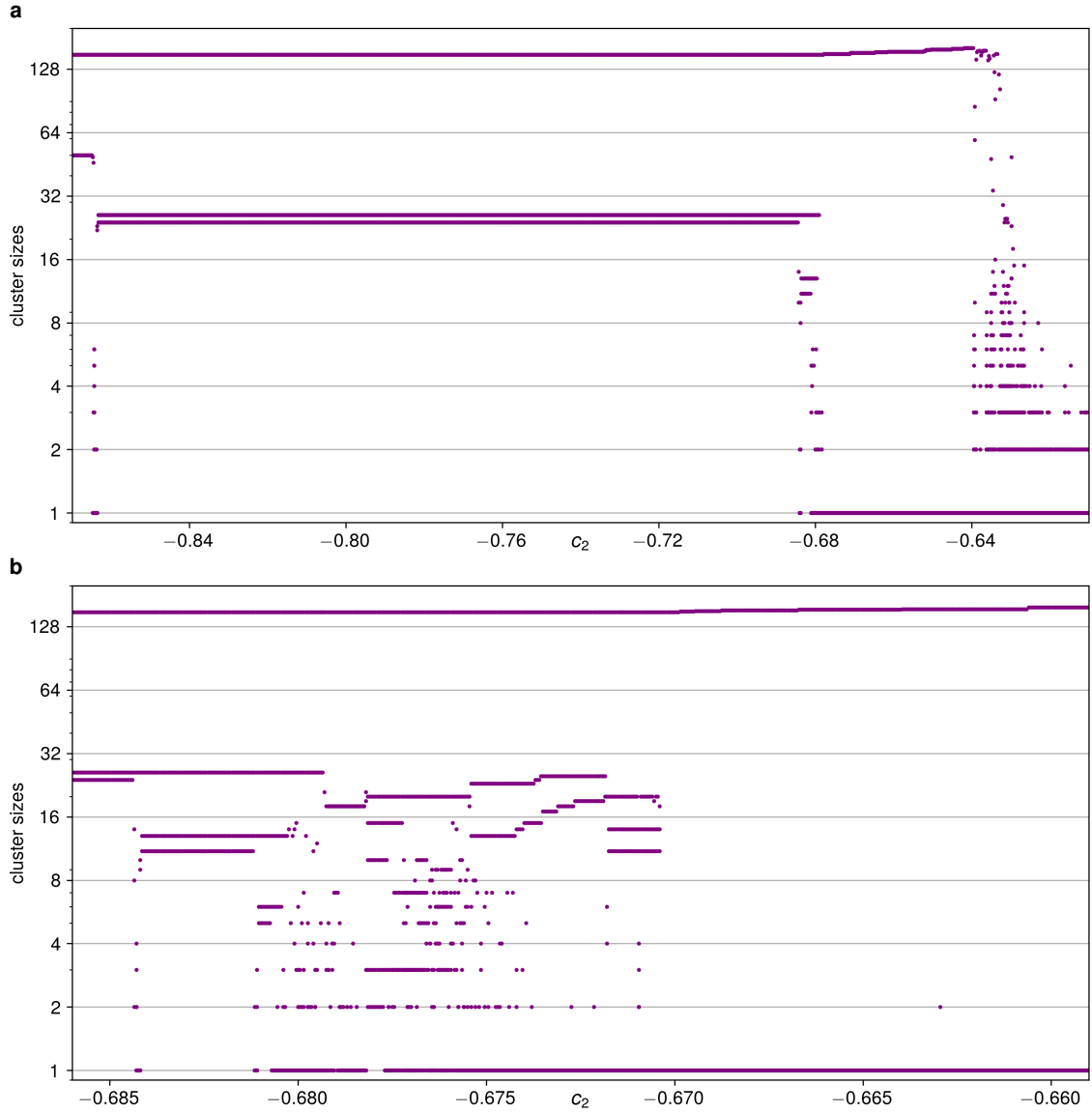
Supplementary Fig. 5. Cluster-splitting cascade and ensuing bifurcations for $N = 32$ and $\eta = 0.67$, starting at 16–16. **a**, All occurring maxima of the real parts $\text{Re}(w_k)$ of all clusters and single oscillators against c_2 as c_2 is gradually increased at a rate of $\Delta c_2 = 2 \cdot 10^{-5}$ every 10^4 time steps. Oscillators are colored by the clusters to which they belong in the cluster-splitting cascade taking up most of the depicted range of c_2 : Initially, there are two clusters of 16, reaching a single maximum shown in green. At $c_2 \approx -0.642$, one of these clusters splits up into a cluster of nine (blue) and a cluster of seven (purple), that both are period-2. At $c_2 \approx -0.6315$, the cluster of seven splits up into a cluster of four (purple) and a cluster of three (yellow). At $c_2 \approx -0.7298$, the cluster of three splits up into a cluster of two (yellow) and a single oscillator (red). When the cluster of two is destroyed, the two resulting single oscillators are shown in red and black. At higher c_2 values, additional single oscillators retain the color of the cluster to which they belonged in the 16–9–4–1–1–1 solution. At $c_2 \approx -0.6282$, the ensemble jumps to the 16–8–4–4 solution. At $c_2 \approx -0.2668$, the cluster of 16 is destroyed and there are henceforth only single oscillators. In this irregular regime, the maxima of $\text{Re}(w_k)$ reach as far down as $\max[\text{Re}(w_k)] = -0.8$. These maxima have been cut off for a clearer view of the dynamics at lower c_2 values. This same final state is also reached from the very different starting point in Supplementary Figure 6. **b**, Cluster sizes at each value of c_2 during the c_2 -incremented simulation in **a**. Calculations are based on cross correlations of trajectories (in the non-rotating frame) over the last 800 time steps of simulation at each c_2 value and a threshold of $\varepsilon = 10^{-8}$. See Methods section.



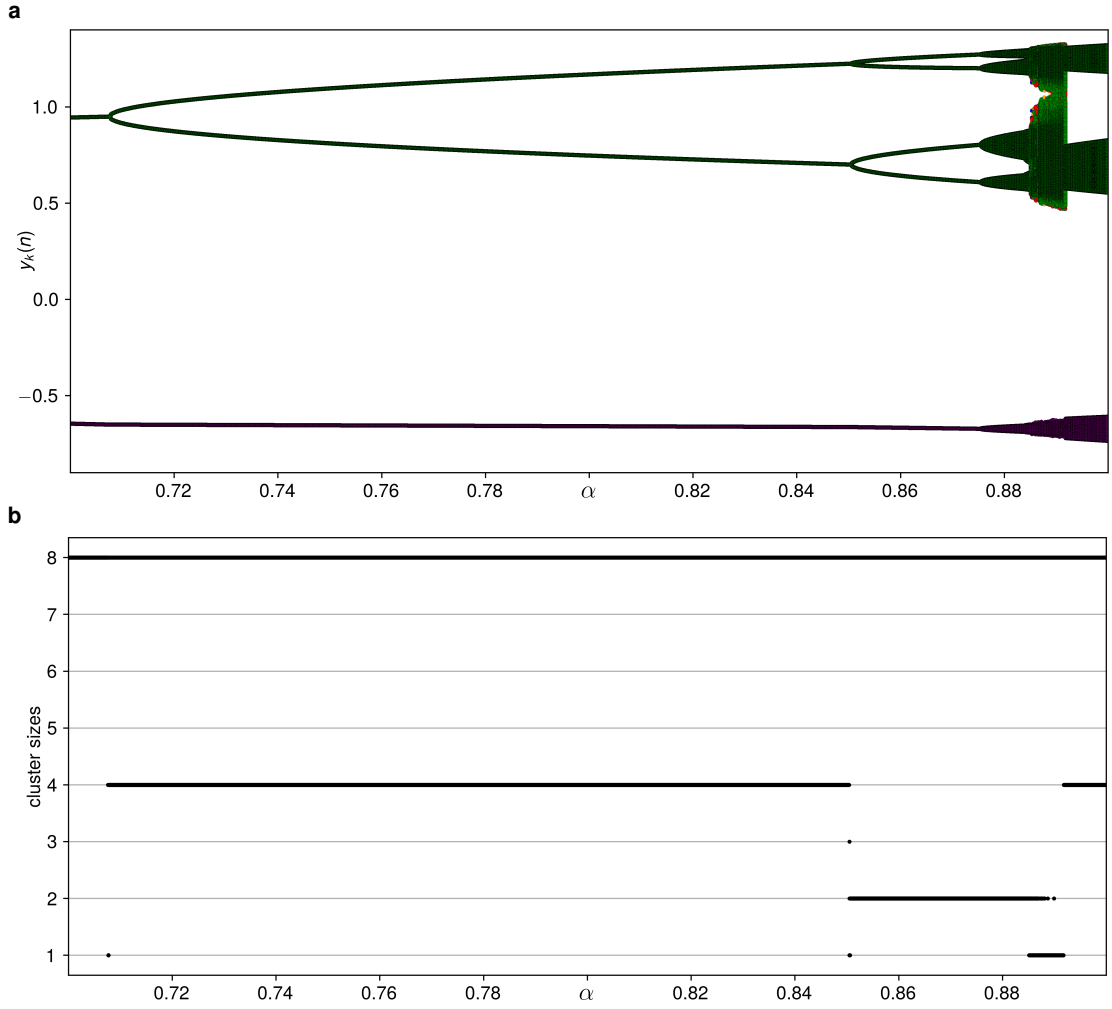
Supplementary Fig. 6. Bifurcations encountered for $N = 32$ and $\eta = 0.67$, when starting at $27-2-1-1-1$ and increasing c_2 . **a**, All occurring maxima of the real parts $\text{Re}(w_k)$ of all clusters and single oscillators against c_2 as c_2 is gradually increased at a rate of $\Delta c_2 = 2 \cdot 10^{-5}$ every 10^4 time steps for $N = 32$, $\nu = 0.1$ and $\eta = 0.67$. The initial state is a $27-2-1-1-1$ quasiperiodic solution, with maxima of the cluster of 27 shown in blue, those of the cluster of two in grey and those of the three single oscillators, which all pursue the same solution, in red. At $c_2 \approx -0.6402$, a torus bifurcation breaks the cluster of 27 into single oscillators, and broadens the formerly discrete maxima into continuous ranges. At $c_2 \approx -0.6364$, this solution undergoes a symmetry-increasing collision to only single oscillators. This final state is also reached from the very different starting point in Supplementary Figure 6. **b**, Cluster sizes at each value of c_2 during the c_2 -incremented simulation in **a**. The further c_2 is increased away from the symmetry-increasing bifurcation, the less distinct do the ruins of the former ordered state become and the less likely are many of the oscillators to cluster at any given time. Calculations are based on cross correlations of trajectories (in the non-rotating frame) over the last 800 time steps of simulation at each c_2 value and a threshold of $\varepsilon = 10^{-8}$. See Methods section.



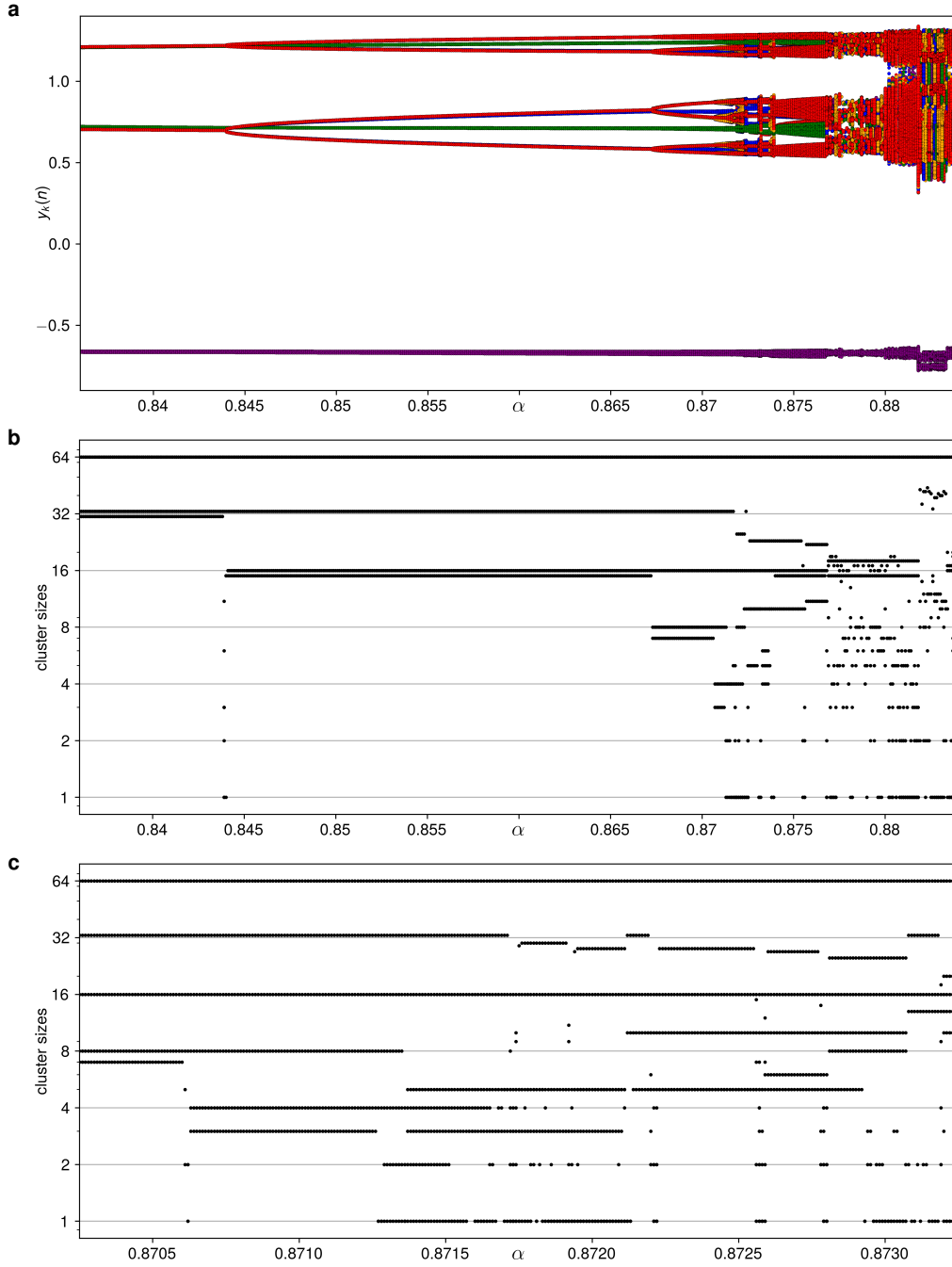
Supplementary Fig. 7. Solutions encountered along the simulation in Supplementary Fig. 6. **a**, Complex-plane portrait of the 27-2-1-1-1 solution at $c_2 = -0.642$. The cluster of 27 two is shown in blue, the cluster of two in grey and the three single oscillators in red, green and yellow, respectively. In order not to obscure its trajectory, the blue dot marking the instantaneous location of the cluster of 27 is smaller than 27 times as large as the dots marking the single oscillators. **b**, Time series of the real part of each cluster and oscillator in **a**. **c,d**, Like **a,b** for the 2-(30x1) state found at $c_2 = -0.638$, past the torus bifurcation in Supplementary Figure 6. Here, the single oscillators from the former cluster of 27 are all still plotted in blue. **e,f**, Solution without permanent clusters at $c_2 = -0.625$. Here, eight different colors are arbitrarily used to depict the $N = 32$ different oscillator trajectories, with four oscillators of each color. Thus, line segments of the same color do not necessarily belong to the same oscillator. In the depicted interval, the ensemble has moved both close to ruins of the former 27-2-1-1-1 branch and to ruins of the 16-16 branch, as indicated by the two blue-green loops similar to those of the solutions in Fig. 2 of the main article.



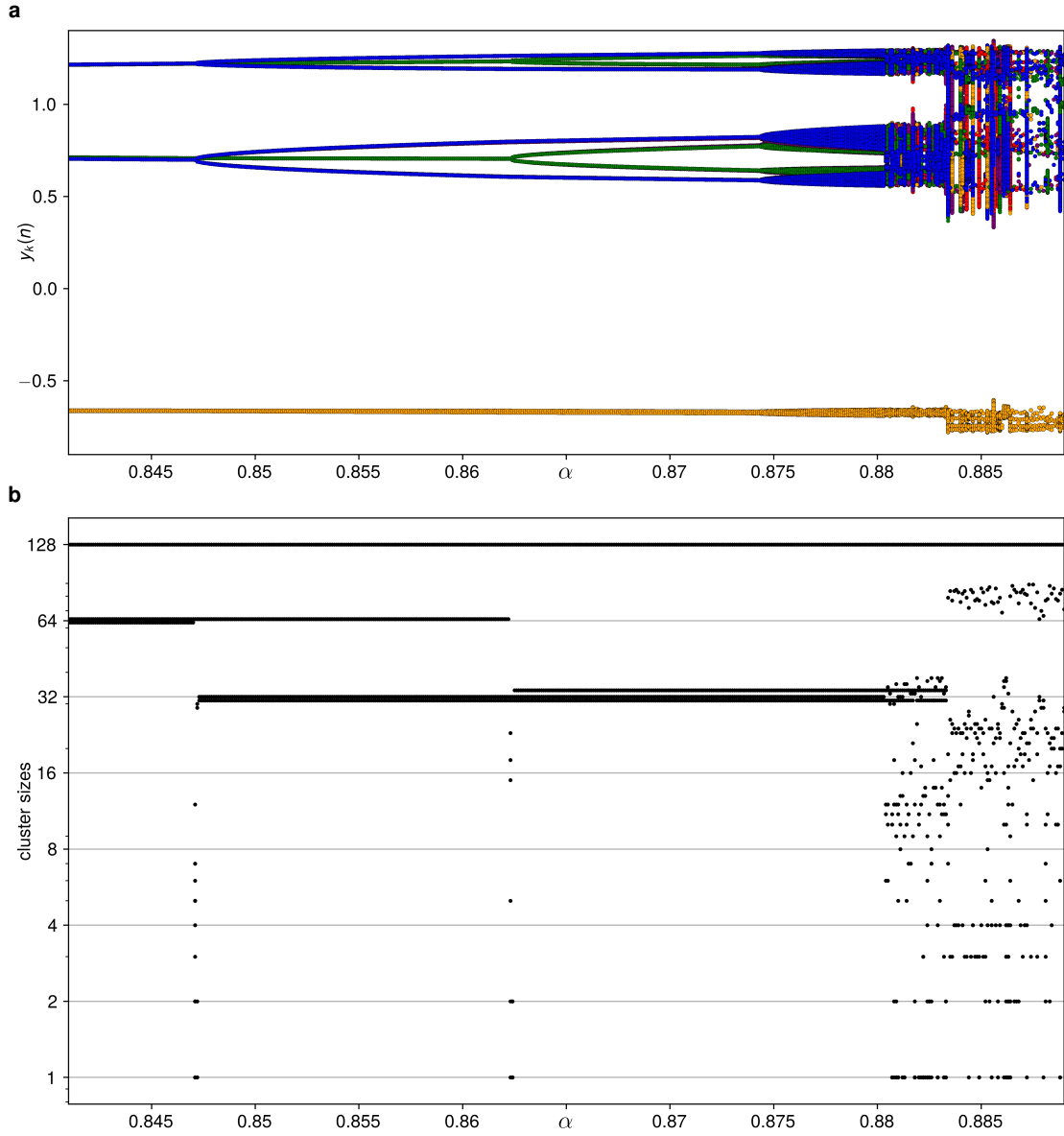
Supplementary Fig. 8. Cluster sizes recorded along the path from a 150–50 solution to chimera state. **a**, Occurring cluster sizes among $N = 200$ oscillators as c_2 is gradually incremented by $\Delta c_2 = 2 \cdot 10^{-4}$ every 2100 time steps at $\nu = 0.1$ and $\eta = 0.67$. Two oscillators are counted as being in the same cluster if their correlation distance in the interval from $t = 2000$ to $t = 2100$ at the relevant value of c_2 is less than 10^{-10} . Note that the vertical axis scales logarithmically. **b**, Analogue to **a**, but for a shorter c_2 interval and with a smaller increment $\Delta c_2 = 5 \cdot 10^{-5}$ and longer simulation time of 4200 time steps at each c_2 value. In both **a** and **b**, the initial cluster splittings are accompanied by transient many-cluster solutions that are not allowed to subside before the number of clusters is calculated. This causes the temporary increase in recorded small clusters at the beginning of each step of the cascade. Some of the multi-cluster solutions at higher values of c_2 could thus also be transients.



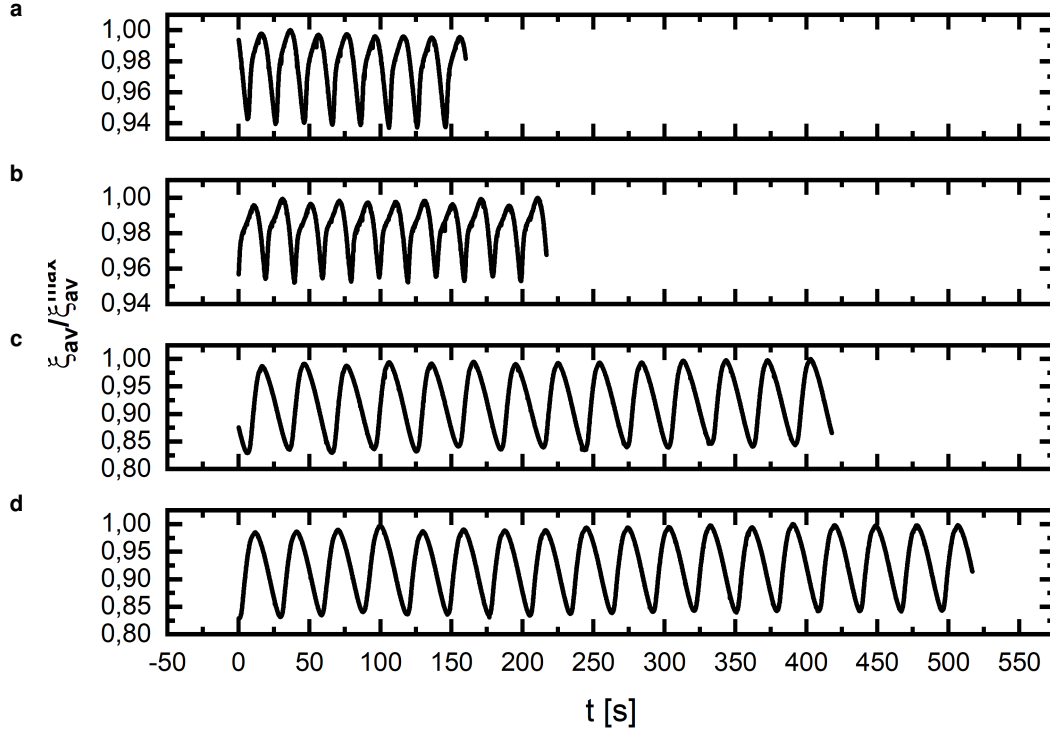
Supplementary Fig. 9. α -incremented simulation of $N = 16$ globally coupled pitchfork maps for $\beta = 0.15$. **a**, All occurring values $y_k(n)$ of all clusters and single maps against α as α is gradually increased at a rate of $\Delta\alpha = 10^{-4}$ every 10^4 iterations of the maps. The values $y_k(n) < -0.5$ are reached by a non-splitting cluster of eight. The leftmost values ≈ 1.0 are reached by the other initial cluster of eight. At $\alpha \approx 0.71$, this cluster splits into two smaller of size four, both pursuing the same period-2 trajectory. At $\alpha \approx 0.85$, each of these clusters splits into two even smaller clusters of size two, henceforth pursuing the same period-4 trajectory. At $\alpha \approx 0.875$, a Neimark-Sacker bifurcation takes place, not affecting the cluster sizes. Somewhat above $\alpha = 0.88$, the clusters of two are broken in a symmetry-increasing bifurcation, resulting in itinerant motion. Even further upward in α , the system transitions to a 8–4–4 quasiperiodic solution. **b**, Cluster sizes at each value of α during the α -incremented simulation in **a**. To calculate the cluster sizes for a certain value of α , the time series containing the 2000 last increments of each map at that value of α are compared pairwise. Two maps are said to be in the same cluster if the Euclidean distance between their 2000-dimensional time vectors is less than $\varepsilon = 10^{-4}$.



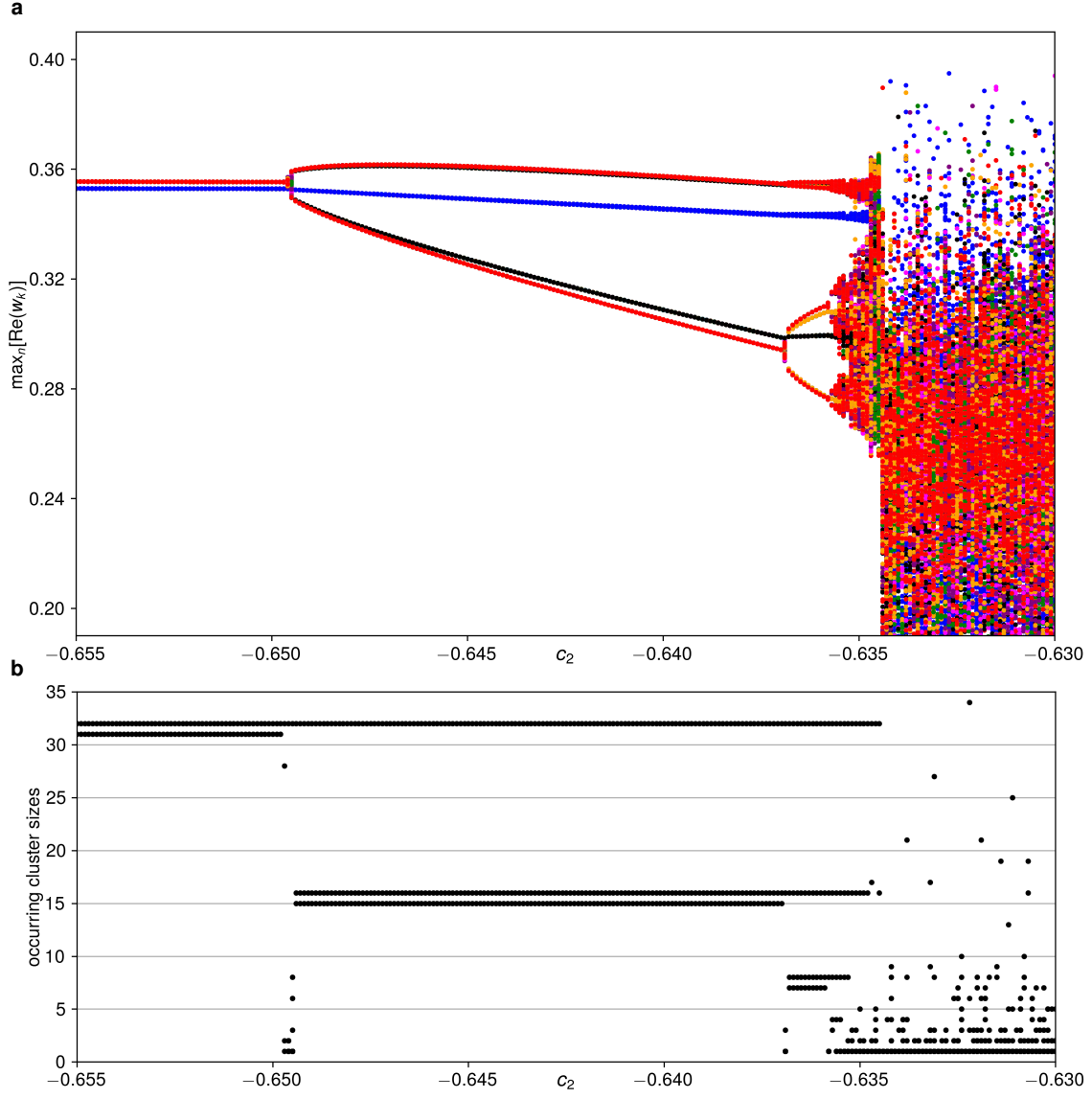
Supplementary Fig. 10. α -incremented simulation of $N = 128$ globally coupled pitchfork maps for $\beta = 0.15$. **a**, All occurring values $y_k(n)$ of all clusters and single maps as α is gradually increased at a rate of $\Delta\alpha = 10^{-4}$ every 10^4 iterations n of the maps. The initial cluster-size configuration is 64–33–31. The values $y_k(n) < -0.5$ are reached by the cluster of 64. In the very left, values of the cluster of 33 are shown in green, those of the cluster of 31 in red. At $\alpha \approx 0.844$, the cluster of 31 splits into a cluster of 16 (blue) and a cluster of 15 (red). At $\alpha \approx 0.867$, the cluster of 15 splits into a cluster of 8 (red) and a cluster of 7 (yellow). At $\alpha \approx 0.870$, the cluster of 7 splits into a cluster of 4 and a cluster of 3. **b**, Cluster sizes at each value of α during the simulation in **a**. Cluster sizes are calculated like in Supplementary Fig. 9. **c**, Cluster sizes during a more finely α -incremented simulation, initialized in the 64–33–16–8–7 solution from **c**, with α increased by $\Delta\alpha = 10^{-5}$ every 10^4 iterations n of the maps. This shows that a stable 64–33–16–8–4–2–1 is indeed reached around $\alpha = 0.8713$ before the larger clusters are split.



Supplementary Fig. 11. α -incremented simulation of $N = 256$ globally coupled pitchfork maps for $\beta = 0.15$. **a**, All occurring values $y_k(n)$ of all clusters and single maps as α is gradually increased at a rate of $\Delta\alpha = 10^{-4}$ every 10^4 iterations n of the maps. The initial cluster-size configuration is 128–65–63. The values $y_k(n) < -0.5$ are reached by the cluster of 128. In the very left, values of the cluster of 65 are shown in green, those of the cluster of 63 in blue. At $\alpha \approx 0.847$, the cluster of 63 splits into a cluster of 32 (blue) and a cluster of 31 (purple). At $\alpha \approx 0.862$, the cluster of 65 splits into a cluster of 34 (green) and a cluster of 31 (red), without increasing the overall period. The next bifurcation is a Neimark-Sacker bifurcation at $\alpha \approx 0.874$. **b**, Cluster sizes at each value of α during the simulation in **a**. Here it becomes apparent that the Neimark-Sacker bifurcation is followed by two symmetry-increasing bifurcations at higher values of α , one wherein the cluster of 32 and a cluster of 31 is destroyed, and another wherein the other smaller clusters are broken, resulting in a 128–(128 \times 1) balanced chimera state. Cluster sizes are calculated like in Supplementary Fig. 9.



Supplementary Fig. 12. Time-series of the spatial average of the ellipsometric signal, normalised to its maximum ξ_{av}/ξ_{av}^{max} for **a** the anti-phase state, **b** the sub-harmonic cluster state, **c** the chimera state and **d** the turbulent state.



Supplementary Fig. 13. Cluster-splitting cascade and ensuing bifurcations for $N = 63$. **a**, All occurring maxima of the rotating-frame real parts $\text{Re}(w_k)$ of all clusters and single oscillators against c_2 as c_2 is gradually increased at a rate of $\Delta c_2 = 10^{-4}$ every 5000 time steps for $N = 63$, $\nu = 0.1$ and $\eta = 0.67$. Oscillators are colored by the clusters to which they belong in the cluster-splitting cascade. Initially, there is a cluster of 32, reaching a single blue maximum and a cluster of 31 reaching a single red maximum. At $c_2 \approx -0.65$, the latter splits up into a cluster of 16, shown in black, and a cluster of 15, shown in red, that both are period-2. At $c_2 \approx -0.637$, the cluster of 15 splits up into a cluster of eight (yellow) and a cluster of seven (red). At $c_2 \approx -0.6365$, the cluster of seven splits up into a cluster of four (purple) and a cluster of three (red). **b**, Cluster sizes at each value of c_2 during the c_2 -incremented simulation in **a**. Calculations are based on the cross correlations of trajectories (in the non-rotating frame) over the last 800 time steps of simulation at each c_2 value and a threshold of $\varepsilon = 10^{-8}$. See Methods section.